



Horizon 2020  
Programme

**CORTEX**

*Research and Innovation Action (RIA)*

This project has received funding from the European Union's Horizon 2020 research and innovation programme under grant agreement No 754316.

Start date : 2017-09-01 Duration : 48 Months  
<http://cortex-h2020.eu>

1



---

**Experimental report of the 1st campaign at AKR-2 and CROCUS**

---

Authors : Dr. Vincent LAMIRAND (EPFL), Mathieu Hursin (EPFL), Adolfo Rais (EPFL), Sebastian Hübner (TUD), Carsten Lange (TUD), Joachim Pohlus (ISTec), Uwe Paquee (ISTec), Chistoph Pohl (TIS), Oskari Pakari (EPFL), Axel Laureau (EPFL)

CORTEX - Contract Number: 754316

Core monitoring techniques and experimental validation and demonstration Foivos MARIAS

Document title	Experimental report of the 1st campaign at AKR-2 and CROCUS
Author(s)	Dr. Vincent LAMIRAND, Mathieu Hursin (EPFL), Adolfo Rais (EPFL), Sebastian Hübner (TUD), Carsten Lange (TUD), Joachim Pohlus (ISTec), Uwe Paquee (ISTec), Chistoph Pohl (TIS), Oskari Pakari (EPFL), Axel Laureau (EPFL)
Number of pages	56
Document type	Deliverable
Work Package	WP02
Document number	D2.1
Issued by	EPFL
Date of completion	2018-12-03 11:17:18
Dissemination level	Public

---

## Summary

In the framework of the CORTEX project, the work package 2 targets the generation of high quality neutron noise experimental data for the subsequent validation of computer methods and models developed in work package 1. The AKR-2 reactor at TUD, and the CROCUS reactor at EPFL, are the experimental facilities where noise-specific experimental data are being generated. This report documents the experimental setup and measurements for each perturbation type and facility. An in-depth characterization of the whole acquisition chain was also performed in the framework of the qualification and comparison of the acquisition systems of TUD and EPFL, with regards to the industry-graded ISTec system (subtask 2.1.1).

---

## Approval

Date	By
2018-12-03 12:33:22	Mr. Mathieu HURSIN (EPFL)
2018-12-03 12:35:12	Pr. Christophe DEMAZIERE (Chalmers)

# Table of contents

Index of Tables .....	1
Index of Figures .....	2
Abbreviations .....	3
Summary .....	4
1 Overview .....	5
2 AKR-2 first experimental campaign .....	5
2.1 The AKR-2 reactor .....	5
2.2 Neutron detection instrumentation .....	6
2.3 Measurements .....	8
3 CROCUS first experimental campaign .....	15
3.1 The CROCUS reactor .....	15
3.2 The COLIBRI experimental setup .....	16
3.3 Measurements .....	20
4 Qualification of data acquisition systems .....	23
4.1 Description of the acquisition systems .....	23
4.2 Benchmarking and qualification of data acquisition systems .....	28
5 Conclusion .....	39
6 References .....	40
7 Appendices .....	41
7.1 AKR-2 reactor data summary .....	41
7.2 AKR-2 reactor kinetic data .....	42
7.3 AKR-2 detectors position .....	43
7.4 Neutron measurement channels for the AKR-2 campaign .....	45
7.5 Specifications of the detectors of the AKR-2 campaign .....	46
7.6 Reactivity worth of AKR-2 perturbation systems .....	47
7.7 Neutron measurement channels for the CROCUS campaign .....	48
7.8 Specifications of the detectors of the CROCUS campaign .....	49
7.9 Scripts for data acquisition benchmark .....	52

## Index of Tables

Table 1 – Detectors specifications and locations with respect to the MCNP model coordinates. All coordinates are given for the centre of the effective zone of the detectors. Angular and radial positions are indications for representation in the horizontal plane (see Figure 2).....	7
Table 2 – AKR-2 measurement channels and signals .....	8
Table 3 – List of the rotating absorber measurements performed with each system. ....	11
Table 4 – List of the vibrating absorber measurements for each system. ....	14
Table 5 – Detectors specifications and locations with respect to the MCNP model coordinates. In italic, location coordinates within the lattice. ....	20
Table 6 – Measurements list with corresponding reactor state (including final position of control rod, and water level oscillations' amplitude), and oscillation specifications (amplitude, frequency, and ID).....	21
Table 7 – Downsampling effect on peak amplitude estimation – Rotating absorber exp. 1.....	33
Table 8 – Benchmarking results for rotating absorber experiments. ....	34
Table 9 – Benchmarking results for vibrating absorber experiment. ....	35
Table 10 - Benchmarking results for the CROCUS vibrating fuel rods experiments .....	37
Table 11 – AKR-2 reactor kinetic data.....	42
Table 12 - AKR-2 reactor kinetic data – 6-group delayed neutron data. ....	42



*This project has received funding from the Euratom research and training programme 2014-2018 under the grant agreement n°754316*

Table 13 – Dimensions of AKR-2 fission chambers and compensated ionization chambers. ....	46
Table 14 – Measured reactivity of the rotating absorber. ....	47
Table 15 – Measured reactivity of the linear moving absorber. ....	47
Table 16 – Specifications of the BF <sub>3</sub> proportional counters, from the supplier in the case of the Transcommerce International MN-1 detector, measured (casing) and estimated (active) for the “grey” smaller detector. ....	50

## Index of Figures

Figure 1 – Cross section of the AKR-2 reactor. ....	6
Figure 2 – Cross section of the AKR-2 reactor showing components and nuclear instrumentation. ....	7
Figure 3 – Absorber location in rotating absorber experiments. Cross-section at 138 cm height from ground or +8 cm from reactor core center. ....	9
Figure 4 – Geometrical description of rotating absorber. Cross and longitudinal views, units in cm. ....	9
Figure 5 – Rotating absorber position signal for EPFL_8 measurement. ....	10
Figure 6 – In blue, absorber location with regards to the core in vibrating absorber experiments. Top view. ....	12
Figure 7 – Absorber motion path inside channel 1-2. Side view. Units in cm. ....	12
Figure 8 – Trapezoidal motion followed by absorber in vibrating absorber experiments. ....	13
Figure 9 – Vibrating absorber position signal for measurement #22. ....	13
Figure 10 – Overview of the CROCUS reactor in a reference configuration. Note: The COLIBRI fuel rods oscillation device is thus not shown. ....	15
Figure 11 – COLIBRI fuel rods oscillator alone (left) and with core structures (right), and a few rods inserted in the device. ....	16
Figure 12 – Cross section of the modified superior grid: enlarged holes in COLIBRI's region and thicker cadmium layer (1 mm). ....	16
Figure 13 – Cross section of the modified inferior grid: enlarged holes in COLIBRI's region and thicker cadmium layer (1 mm). ....	17
Figure 14 – Side cross section of the oscillator with only two fuel rods inserted in it; one fuel rod is in its static configuration laying at the bottom (left), the other one is lifted up 10 mm for oscillation. ....	17
Figure 15 – Details of the control and monitors of the oscillation: (left) Motor on its rotation axis; (center) Close-up on the rotation axis with focus (blue) on the inductive captor detecting one of the four pins; (right) Measuring cable and close-up (blue) on its connection at the bottom to the transmission aluminum beam. ....	18
Figure 16 – Typical inductive captor (bottom, red) and cable (top, blue) signals, here in the case of one rod oscillating in air at $\pm 1.5$ mm and 1 Hz. In yellow, ideal sinusoidal oscillation for comparison with the real and measured displacement. ....	18
Figure 17 – Comparison of the oscillator behavior at the bottom position for 1 and 18 rods loads in water (1000 mm), as compared to the device oscillating empty loaded in air (i.e. expected to be equivalent to the behavior of the top part). All measurements were carried out using the cable coder. ....	19
Figure 18 – Experimental locations of detectors, with their ID, details and instrumentation channel. ....	20
Figure 19 – ISTec SIGMA data acquisition system (left) connected to five ROBOTRON units (right). ....	23
Figure 20 – Measurement scheme of ISTec DAQ SIGMA. ....	25
Figure 21 – EPFL data acquisition system. ....	26
Figure 22 – Measurement scheme of EPFL/PSI pulse mode acquisition system. ....	26
Figure 23 – On the left, schematic of the in-house developed current amplifier connected to a typical large FC Photonis CFUL01, such as those used during the CROCUS campaign (detectors 5 and 6); on the right, schematic of the instrumentation channels connected to the oscilloscope used as acquisition system for current mode measurements. ....	26
Figure 24 – Measurement scheme of TUD acquisition system. ....	27
Figure 25 – AKR-2 detection chain for DAQ benchmarking. ....	28

Figure 26 – Uncertainty quantification process for peak power estimation. ....	30
Figure 27 – EPFL and TUD z-scores a function of M scaling factor, rotating absorber exp. 2. ....	31
Figure 28 – EPFL and TUD z-scores a function of M scaling factor, vibrating absorber exp. 14. ....	31
Figure 29 – Power density spectrum for vibrating absorber exp. 22 - Detector 1. ....	32
Figure 30 – Power spectral density for COLIBRI exp. 3 - Detector 6 (current mode). ....	32
Figure 31 – Power spectral density for rotating absorber exp. 1 – No downsampling for EPFL. ....	33
Figure 32 – Time series data from TUD and EPFL systems for rot. abs. exp. 2. ....	35
Figure 33 – Frequency distribution of EPFL and TUD z-scores for all experiments. ....	37
Figure 34 – Section of the Lower Tangential Channel (5-6) of the AKR-2. ....	43
Figure 35 – Position of Detector 1. ....	43
Figure 36 – Position of Detector 2. ....	43
Figure 37 – Section of the Central Channel (1-2) of the AKR-2. ....	43
Figure 38 – Position of Detector 3. ....	44
Figure 39 – Neutron measurement channels for the AKR-2 campaign. ....	45
Figure 40 – Schematic of the <sup>3</sup> He proportional counters, i.e. detectors 1 to 3, used in the channels 5, 6 and 2, respectively. ....	46
Figure 41 – Measured reactivity of the rotating absorber. ....	47
Figure 42 – Measured reactivity of the linear moving absorber. ....	47
Figure 43 – Neutron measurement channels for the CROCUS campaign. ....	48
Figure 44 – Schematic of the Photonis CFUL01 fission chamber. ....	49
Figure 45 – Schematic of the fission chamber tube and in-air experimental channel with respect to the superior grid. NB: the channel is set vertically in-core, left side is top. ....	49
Figure 46 – X-ray image of a Transcommerce International MN-1 detector. ....	50
Figure 47 – Schematic of the in-air aluminum experimental channel used by one MN-1 and both “grey” BF <sub>3</sub> proportional counters, with respect to the grids and the reactor base plate. NB: the channel is set vertically in-core, left side is top. ....	50
Figure 48 – Schematic of the Photonis CFUF34 miniature fission chamber. NB: the detector’s side is at the bottom when set in-core. ....	51

## Abbreviations

AC	Alternating Current
CIC	Compensated Ionization Chamber
COLIBRI	CROCUS Oscillator for Lateral Increase Between u-metal Rods and Inner zone
DAQ	Data acquisition system
DC	Direct Current
ECCP	Electronic Collaborative Content Platform
EPFL	Ecole Polytechnique Fédérale de Lausanne
FC	Fission chamber
FFM	Fix Filter Module
FFT	Fast Fourier Transform
ISTec	TÜV Rheinland ISTec GmbH – Institut für Sicherheitstechnologie
MFC	Miniature Fission Chamber
PC	Proportional Counter
PRM1	linear Power-Range channel Monitor 1
PSD	Power Spectral Density
SAD	Simultaneous Analog-Digital converter
TTL	Transistor-Transistor Logic
TUD	Technische Universität Dresden
U <sub>metal</sub>	Metallic uranium
UO <sub>2</sub>	Uranium oxide
WP	Work package
WRM	Wide-Range channels Monitor (WRM1 and WRM2)

## Summary

In the framework of the CORTEX project, the work package 2 targets the generation of high quality neutron noise experimental data for the subsequent validation of computer methods and models developed in work package 1. The AKR-2 reactor at TUD, and the CROCUS reactor at EPFL, are the experimental facilities where noise-specific experimental data are being generated.

This report documents the experimental setup and measurements for each perturbation type and facility. An in-depth characterization of the whole acquisition chain was also performed in the framework of the qualification and comparison of the acquisition systems of TUD and EPFL, with regards to the industry-graded ISTec system (subtask 2.1.1).

The noise experimental data will be distributed to the members of the consortium in the form of raw time series and a few examples of power spectral densities.

## 1 Overview

The CORTEX project aims at developing an innovative core monitoring technique that allows detecting anomalies in nuclear reactors, such as excessive vibrations of core internals, flow blockage, coolant inlet perturbations, etc. The technique will be based on primarily using the inherent fluctuations in neutron flux recorded by in-core and ex-core instrumentation, from which the anomalies will be differentiated depending on their type, location and characteristics. The method is non-intrusive and does not require any external perturbation of the system. The project will result in a deepened understanding of the physical processes involved. This will allow utilities to detect operational problems at a very early stage and to take proper actions before such problems have any adverse effect on plant safety and reliability.

The main purpose of the experimental campaigns at the AKR-2 and CROCUS reactors is to produce high quality noise-specific experimental data for the validation of the neutron noise computational models. A second objective associated with the high-quality target of the data is to qualify EPFL and TUD acquisition systems by cross-comparing them with regards to the industry-graded ISTec SIGMA system.

The present document is structured in three main sections: a first one describing the experimental campaign at the AKR-2 reactor, a second one describing the first experimental campaign at the CROCUS reactor and a last one reporting the results of the qualification of the data acquisition systems (subtask 2.1.1). Following this report, all experimental data will be distributed to all partners in the form of time series identified by their measurement number, instrumentation, and signal's number, e.g. AKR2\_1\_I\_2 for the acquisition of ISTec instrumentation of detector 2 during the first measurement in AKR-2.

## 2 AKR-2 first experimental campaign

The first experimental campaign in the AKR-2 reactor took place from 6 to 15 March 2018. Two types of experiments were carried out to induce neutron flux oscillations: rotation of a thermal neutron absorber (of variable absorption cross-section with respect to the rotation angle) and linear moving of an absorber oscillating back and forth in the reactor core (a.k.a. vibrating absorber). This section begins with a description of the AKR-2 reactor and it later provides the details of the experimental setup and procedure for these measurements.

### 2.1 The AKR-2 reactor

The AKR-2 reactor of the TU Dresden (TUD) is a thermal, homogeneous, polyethylene moderated zero-power reactor with an allowed maximum continuous (thermal) power of 2 Watt. Currently a maximum of 0.587 Watt is achievable, as the displayed power has a conversion factor of  $3.41 \pm 0.2$  [1]. Power values indicated in the document do not take this factor into account. The core has cylindrical shape with a diameter of 250 mm and a critical height of 275 mm. The disk-shaped fuel elements consist of a homogeneous dispersion of polyethylene and uranium oxide (19.8 % enriched in  $^{235}\text{U}$ , with an O-to-U ratio of 2.27). The  $^{235}\text{U}$  density in the fuel elements amounts to  $0.060 \text{ g/cm}^3$ .

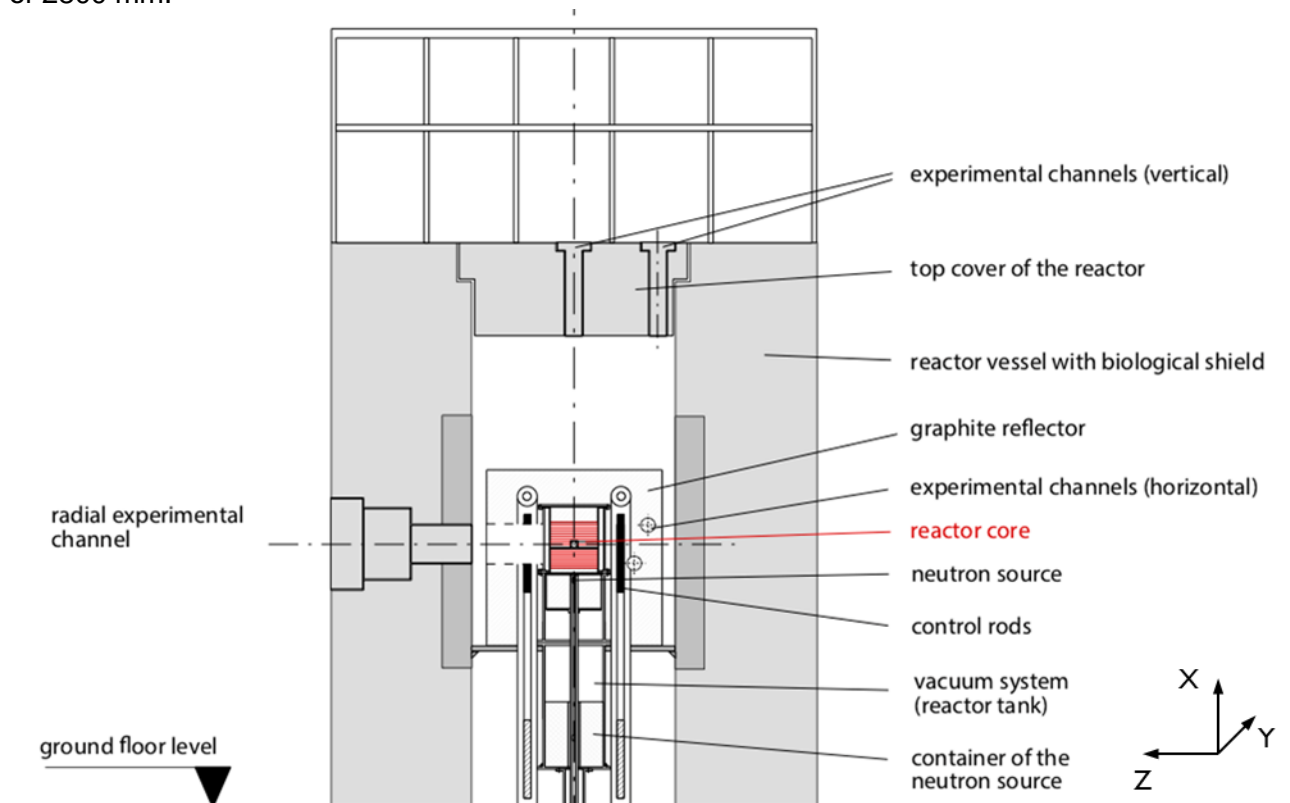
The core is surrounded by a graphite reflector with a density of  $1.75 \text{ g/cm}^3$  (see Figure 1). The axial and radial thicknesses are 20 cm and 32 cm, respectively. Therefore, the critical mass is relatively small (about 790 g of  $^{235}\text{U}$ ). Within certain constraints the AKR-2 is a minimum-critical-mass reactor.

For safety reasons, the core consists of two separable sections. The fuel elements of each section are enclosed in a hermetically sealed aluminum container. In the shut-down position the distance between the lower and the upper core section is about 50 mm. The lower section is lifted by means of a core drive mechanism including an electromagnetic holder of the core section. Through a tube within this mechanism the start-up neutron source (Am-Be, neutron yield  $2.2 \cdot 10^6 \text{ n/s}$ ) is moved from the source container to the bottom side of the core. The distance between the bottom side of the core and the middle of the source container measures about 800 mm.



The reactor is controlled by three cadmium absorber plates. These plates are moved vertically in a gap within the reflector outside the reactor tank. They are designed as combined control and safety rods. An automatic reactor power control is available using the control rods. The lower core section and the control rods are held by electromagnets in their normal-operation positions. Any scram signal opens the direct-pull holding magnets allowing the rods and the lower core section to fall in the shut-down position by gravity.

The reactor core, reactor tank, graphite reflector and control rods are arranged on a horizontal steel plate (diameter 1000 mm, thickness 30 mm) inside the reactor vessel. This is a cylindrical double-walled vessel containing the biological shield and having an outer diameter of 2500 mm and a height of 2800 mm.



**Figure 1 – Cross section of the AKR-2 reactor.**

There are four horizontal and two vertical experimental channels with different diameters and shapes. They provide adequate in-pile irradiation volume with different neutron spectra. At 2 Watt power level the maximum flux density of thermal neutrons in the central experimental channel 1-2 (see Figure 2) is about  $2.5 \cdot 10^7 \text{ n}/(\text{cm}^2 \cdot \text{s})$ .

A summary of the AKR-2 technical parameters and the reactor kinetic data can be found in Appendices 7.1 and 7.2 respectively.

## 2.2 Neutron detection instrumentation

The nuclear instrumentation used for the first campaign measurements at the AKR-2 reactor is comprised by seven detection channels from which the neutron flux level in the reactor is inferred. All detectors are based on prompt processes for neutron conversion and detection. Their specifications and locations are presented in Table 1 and shown in Figure 2 with regards to the MCNP model, which is available on the ECCP. More details on their dimensions is available in Appendix 7.4.

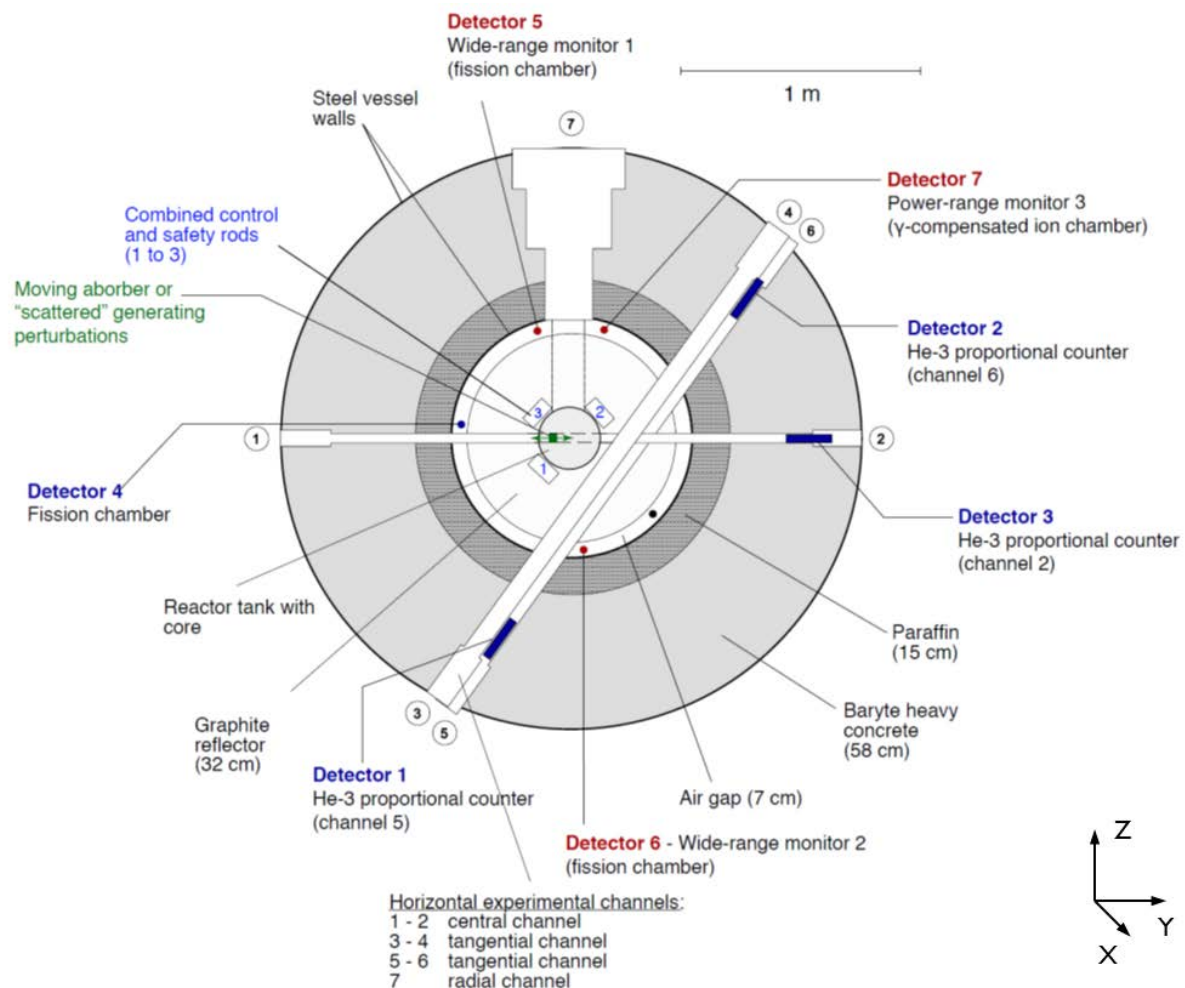


It is worth noting that three of the channels previously mentioned comprise the reactor instrumentation for safety and reactor monitoring purposes. These three detectors are described below and shown in red color in Figure 2.

- 2 logarithmic wide-range channels (WRM1 and WRM2).
- 1 linear power-range channel (PRM1).

**Table 1 – Detectors specifications and locations with respect to the MCNP model coordinates. All coordinates are given for the centre of the effective zone of the detectors. Angular and radial positions are indications for representation in the horizontal plane (see Figure 2).**

#	Type	Sensitive material	X in cm (height)	Y in cm	Z in cm	angle in °	radial in cm
1	PC	$^3\text{He}$ gas	$120 \pm 0.5$	$-40.2 \pm 0.7$	$-82.6 \pm 0.7$	$116.0 \pm 0.2$	$91.9 \pm 1.0$
2	PC	$^3\text{He}$ gas	$120 \pm 0.5$	$82.4 \pm 0.7$	$40.0 \pm 0.7$	$334.1 \pm 0.2$	$91.6 \pm 1.0$
3	PC	$^3\text{He}$ gas	$130 \pm 0.5$	$98.85 \pm 0.1$	$0.0 \pm 0.1$	$0.0 \pm 0.2$	$98.85 \pm 1.0$
4	FC	$^{235}\text{U}$ coating	$130 \pm 2$	$-47.4 \sim 5\%$	$7.5 \sim 15\%$	$189 \pm 3$	$48^{+0.5}_{-1.5}$
5	FC	$^{235}\text{U}$ coating	$130 \pm 2$	$-19.5 \sim 10\%$	$43.9 \sim 5\%$	$246 \pm 3$	$48^{+0.5}_{-1.5}$
6	FC	$^{235}\text{U}$ coating	$130 \pm 2$	$5.0 \sim 20\%$	$-47.7 \sim 5\%$	$84 \pm 2$	$48^{+0.5}_{-1.5}$
7	CIC	$^{10}\text{B}$ coating	$130 \pm 2$	$10.0 \sim 15\%$	$46.9 \sim 5\%$	$282 \pm 2$	$48^{+0.5}_{-1.5}$



**Figure 2 – Cross section of the AKR-2 reactor showing components and nuclear instrumentation.**

## 2.3 Measurements

The experiments at the AKR-2 reactor consisted in introducing two different sources of periodic reactivity perturbations that induce neutron flux oscillations. The first type of perturbation is generated by a rotating neutron absorber that has a varying absorption cross-section with respect to the rotation angle and the second one by a linearly oscillating absorber that is moved back and forth inside the reactor core (vibrating absorber).

The neutron flux levels were measured by seven different out-of-core detectors. In addition to these seven neutron detection signals, three other signals were measured and recorded for the purposes listed below:

- Linearly moving absorber position as a function of time.
- Inductive proximity sensor's signal to detect the rotation speed.
- External TTL signal that is used to synchronize the recorded signals.

Three independent data acquisition systems (DAQ) were provided by TUD, EPFL and ISTec and used during the measurements for signal readout and storage. The signals used during the AKR-2 experiments are listed in Table 2 and their identifiers will be used hereafter in this section of the report. Details concerning the three DAQs can be found in Section 4.1 (Description of the acquisition systems). The complete neutron detection sequence with the associated electronics is represented in Figure 39 of Appendix 7.4. Additional figures on the position of the additional neutron detectors (detectors 1 to 3) inside the reactor for this measurement campaign can be found in Appendix 7.3.

**Table 2 – AKR-2 measurement channels and signals**

	Identifier	Type	Detector model	Location
1	Detector 1	He-3 proportional counter	NEM525A3 Nr. 208	Position: 121 deg. (Channel 5)
2	Detector 2	He-3 proportional counter	NEM525A3 Nr. 207	Position: 329 deg. (Channel 6)
3	Detector 3	He-3 proportional counter	VacuTec typ 70060	Position: 0 deg. (Channel 2)
4	Detector 4	Fission chamber	9R100	Position: 188 deg.
5	Detector 5 - WRM1	Fission chamber	9R100	Position: 251 deg.
6	Detector 6 - WRM2	Fission chamber	9R100	Position: 77 deg.
7	Detector 7 - PRM1	<sup>10</sup> B-coated Ion chamber -Y-compensated	KNK-56	Position: 288 deg.
8	Manual trigger	TTL signal for time synchronization	-	-
9	Rotation sensor	Inductive displacement sensor (screw triggered, screw in line with cadmium foil, no angle phase)	-	-
10	Vibrating absorber. pos. sensor		-	-

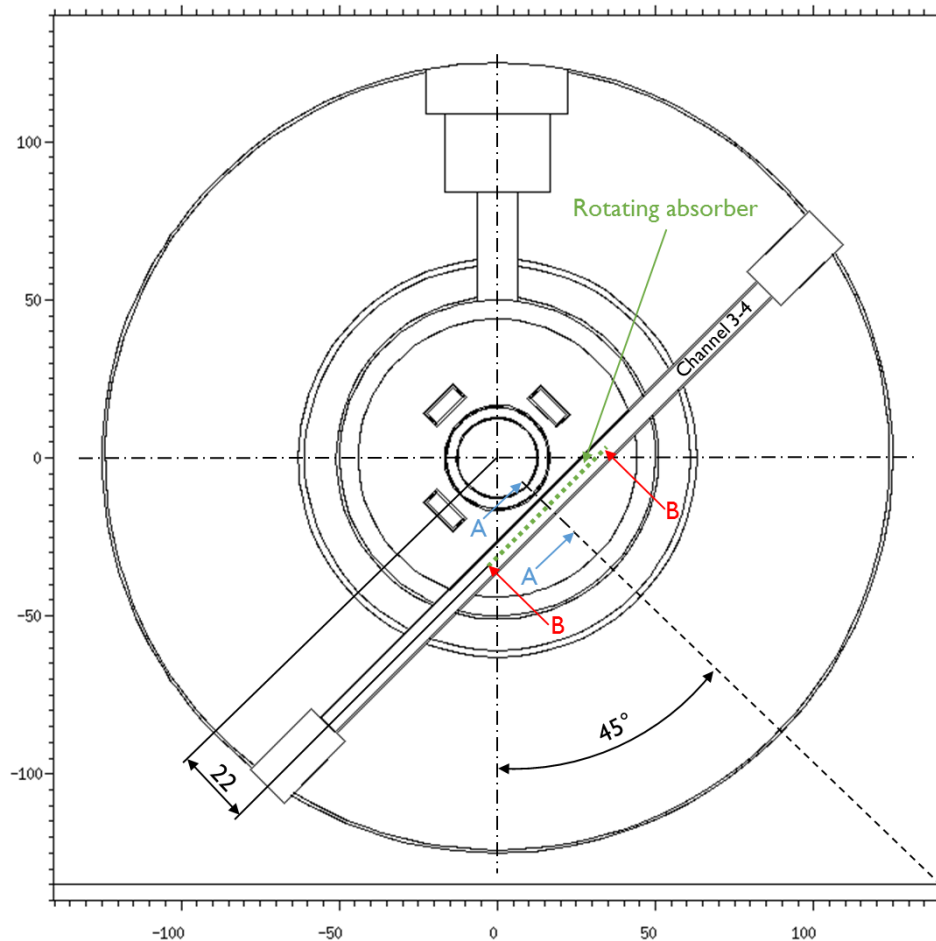
### 2.3.1 Rotating absorber experiments

In order to maximize the perturbation induced to the neutron flux, the rotating absorber shaft was inserted in a location where the gradient of the neutron flux is maximum: i.e., the tangential line (channel 3-4) as illustrated in Figure 3. The reactivity worth of the absorber was measured and is presented in Appendix 7.6.1.

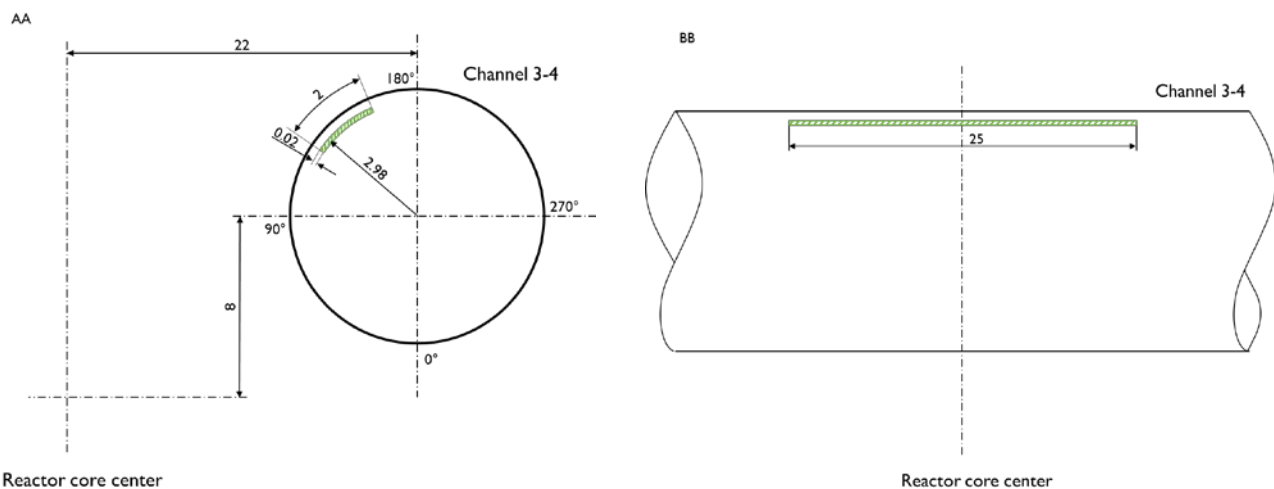
The geometry description and mechanical arrangement of the rotating absorber are summarized below.

- *Absorber material:* natural cadmium (not purified, contains impurities)
- *Dimensions of cadmium sheet (cm):* 25 x 2 x 0.02
- *Rotation axis location:* tangential channel 3-4
- *Rotation axis distance with respect to core center:* 22 cm in the radial direction and 8 cm above in height (see Figure 4).
- *Cadmium sheet location with respect to rotation axis:*  $r_r = 2.98$  cm

The experimental arrangement is illustrated in Figure 3, where a horizontal cross-section of the reactor (at  $z = 8$  cm, measured from the core center) shows the location of the experimental channel and the rotating axis. Figure 4 shows two section views of the rotating absorber (AA and BB) and the geometrical details.

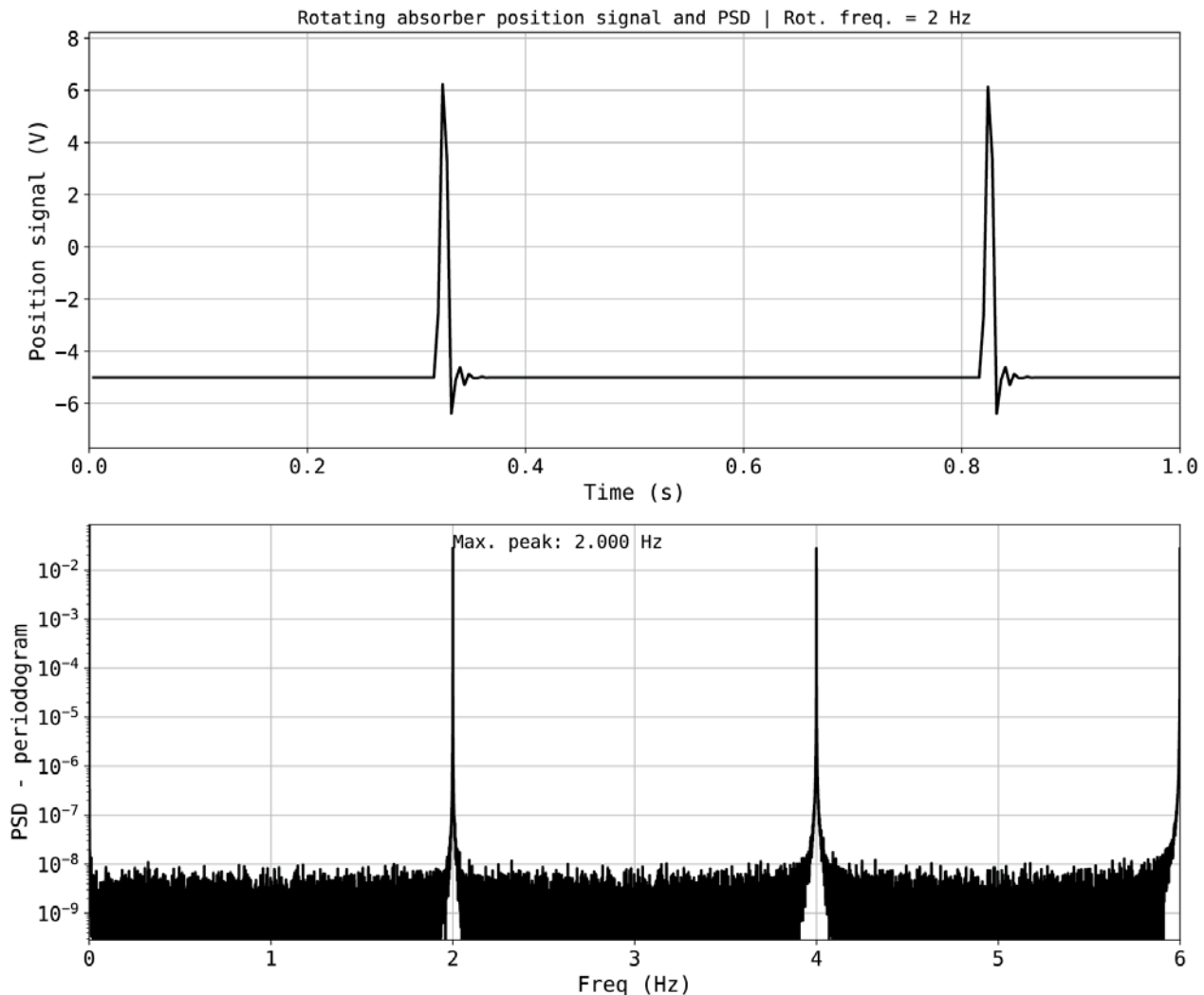


**Figure 3 – Absorber location in rotating absorber experiments. Cross-section at 138 cm height from ground or +8 cm from reactor core center.**



**Figure 4 – Geometrical description of rotating absorber. Cross and longitudinal views, units in cm.**

The rotation was measured by an inductive proximity sensor, which yielded a pulsed signal per revolution as illustrated in the example in Figure 5. The rotation speed was kept constant during each measurement. Figure 5 also shows a power spectral density (PSD) of the position signal measured for 40 minutes with a sampling rate of 4 ms, which verifies that the actual rotation speed corresponds to the one chosen by the software controlling the motor.



**Figure 5 – Rotating absorber position signal for EPFL\_8 measurement.**

Different measurements were taken using a combination of the following parameters:

- Reactor power level. The automatic reactor power control was used during these measurements to maintain the mean value of the fluctuations constant in time.
- Rotation speed
- Sampling rate

The whole set of measurements is listed in Table 3 along with the measurement identifier for each data acquisition system. Note that not all measurements were acquired by the three data acquisition systems due to different complications related to their operation.

Note that for some of the extra measurements, “static” indicate that the absorber was in a static position. The angle was  $0^\circ$  (see angular position in Figure 4) for all these measurements but for the *RA extra 5* measurement, where the rotating absorber was static in an undefined position (indicated with an asterisk \*).

**Table 3 – List of the rotating absorber measurements performed with each system.**

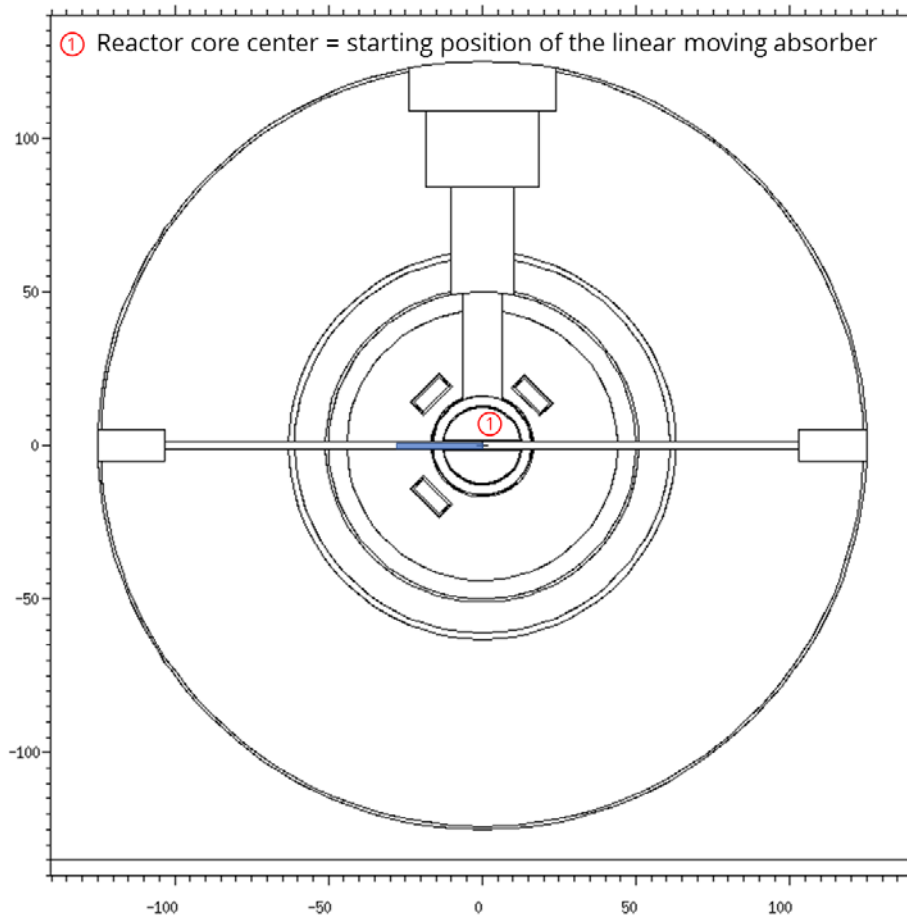
#	Reactor Power (W)	Rot. Frequency (Hz)	ISTec	EPFL	TUD
1	2	2	X	X	
2	2	0,5	X	X	X
3	2	0,2	X	X	X
4	2	0,2	X	X	
5	1	0,2	X	X	
6	1	0,5	X	X	
7	1	1	X	X	
8	1	2	X	X	
9	2	1	X	X	X
10	0,5	1	X	X	X
RA extra 1	1,56	2	X		
RA extra 2	1,6	2	X		
RA extra 3	1,8	2	X		
RA extra 4	2	2	X		
RA extra 5	2	static*	X		
RA extra 6	2	static	X		
RA extra 7	1,5	static	X		
RA extra 8	1	static	X		
RA extra 9	0,8	static	X		
RA extra 10	0,5	static	X		
RA extra 11	0,2	static	X		
RA extra 12	2	1	X		
RA extra 13	1	0,5	X		

### 2.3.2 Vibrating absorber experiments

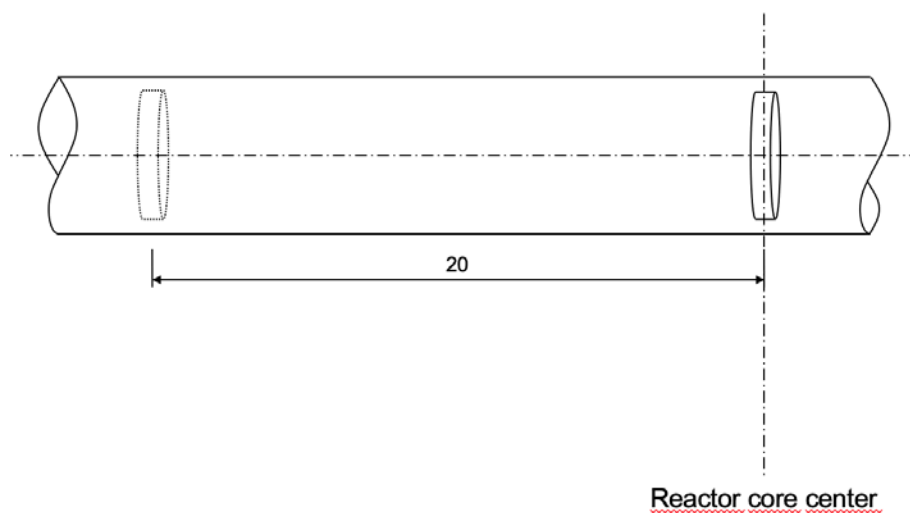
A pneumatic-driven vibrating absorber was employed to linearly oscillate a neutron absorber back and forth inside the reactor core. The absorber is moved along the experimental channel 1-2, between a position inside the core and a position outside the core as illustrated in Figure 6 and Figure 7. The reactivity worth of the absorber was measured and is presented in Appendix 7.6.2.

The material and geometry data for the absorber are summarized below:

- *Linear motion axis*: radial channel 1-2 which is at the same axial level than the core center ( $z = 0$  cm).
- *Absorber thickness*: 1.016 mm
- *Absorber diameter*: 12.7 mm
- *Absorber material*: 99.9656 % nat. Cd; 0.01 % Pb; 0.01 % Cu; 0.01 % Zn; 0.002 % Al; 0.001 % Fe; 0.001 % Ti; 0.0001 % As; 0.0001 % Sb; 0.0001 % Sn; 0.0001 % Ni

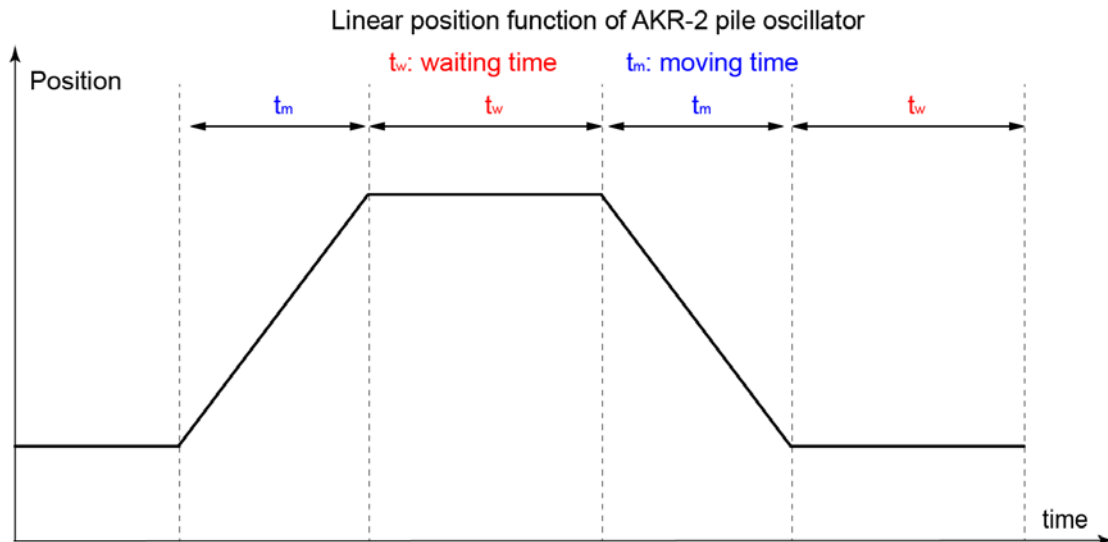


**Figure 6 – In blue, absorber location with regards to the core in vibrating absorber experiments. Top view.**



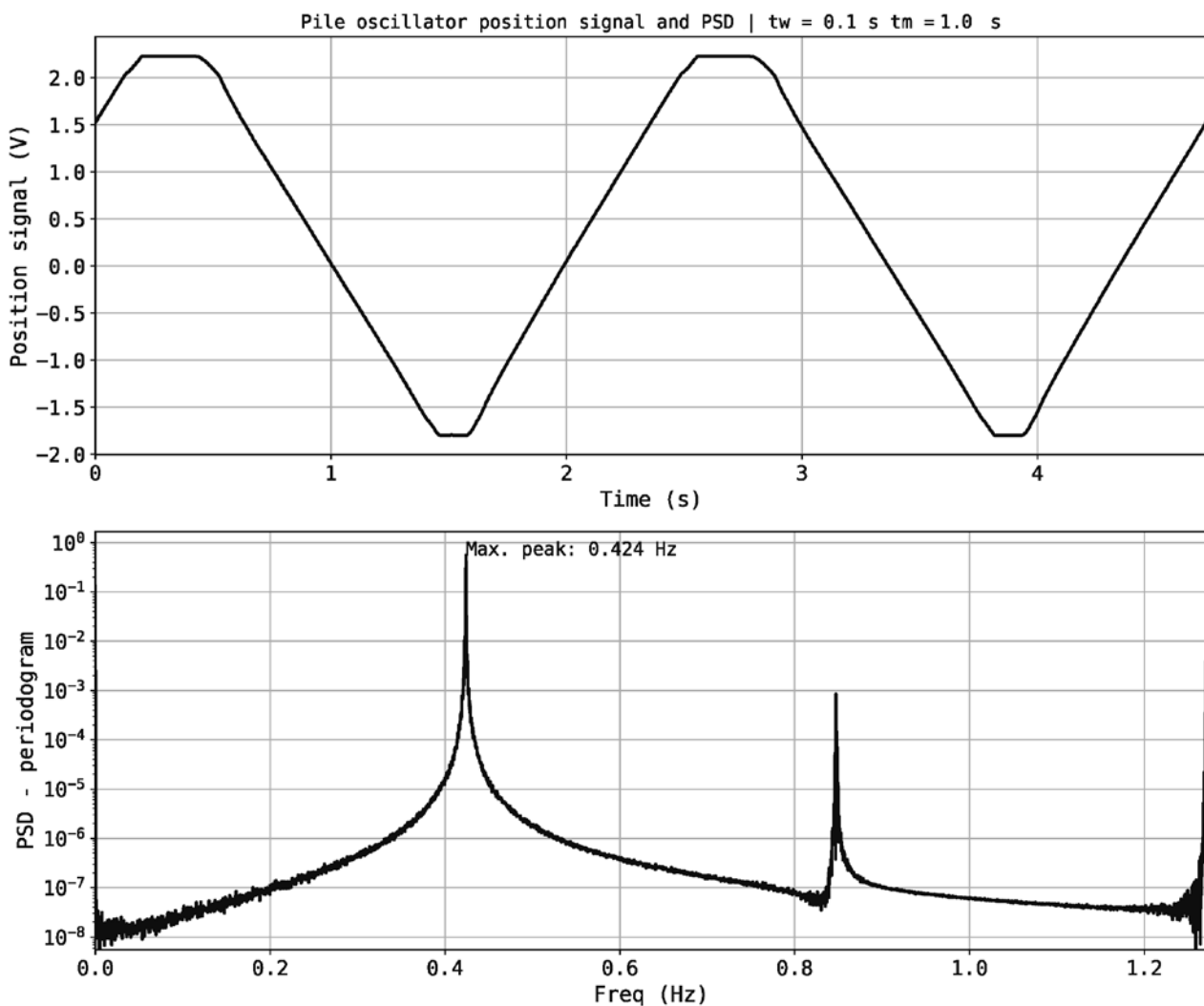
**Figure 7 – Absorber motion path inside channel 1-2. Side view. Units in cm**

The periodic motion of the vibrating absorber is defined by two main parameters: the waiting and moving time as shown in Figure 8. The pneumatic system allows to modify the absorbers motion by varying the moving time ( $t_m$ ) from 0.4 to 2.0 seconds, and/or the waiting time ( $t_w$ ) from 0.1 to 4.0 seconds.



**Figure 8 – Trapezoidal motion followed by absorber in vibrating absorber experiments.**

The relative position of the vibrating absorber was measured during the experiments, yielding a quasi-trapezoidal signal like as shown in Figure 9. The PSD of the position signal is also shown.



**Figure 9 – Vibrating absorber position signal for measurement #22**



Different measurements were taken using a combination of the following parameters:

- Reactor power level: the automatic reactor power control was used during these measurements in order to avoid power drifts.
- Moving time ( $t_m$ )
- Waiting time ( $t_w$ )
- Sampling rate

The list of measurements is shown in Table 4.

**Table 4 – List of the vibrating absorber measurements for each system.**

#	Reactor Power (W)	Motion parameters		ISTec	EPFL	TUD
		$t_w$ (s)	$t_m$ (s)			
11	1	0,1	0,6	X	X	X
12	1	0,4	0,6	X	X	X
13	1	1	0,6	X	X	X
14	0,8	1	0,6	X	X	X
15	2	0,1	0,6	X	X	X
16	2	0,1	1	X	X	X
17	1,9	0,1	2	X	X	X
18	1	0,4	2	X	X	X
19	1	1	2	X	X	X
20	1	2	2	X	X	X
21	1	4	2	X	X	X
22	2	0,1	1	X	X	X
23	2	1	1	X	X	X
24	2	0,4	0,4	X	X	X
25	2	0,4	0,4	X	X	X
26	2	2	0,4	X	X	X
27	2	2	0,4	X	X	
PO Extra 11	1	0,1	0,6	X		X

### 2.3.3 Uncertainties in measurements

The identified uncertainties list as follows:

- Reactor operation:
  - o power: not evaluated
- Perturbation systems:
  - o absorbers' position
  - o absorber materials composition
- Detection:
  - o detectors' location: varying, cf. Table 1
  - o detectors' dimensions: cf. Appendix 7.5
  - o signal: statistical for counts, to be extracted from the raw data more generally.

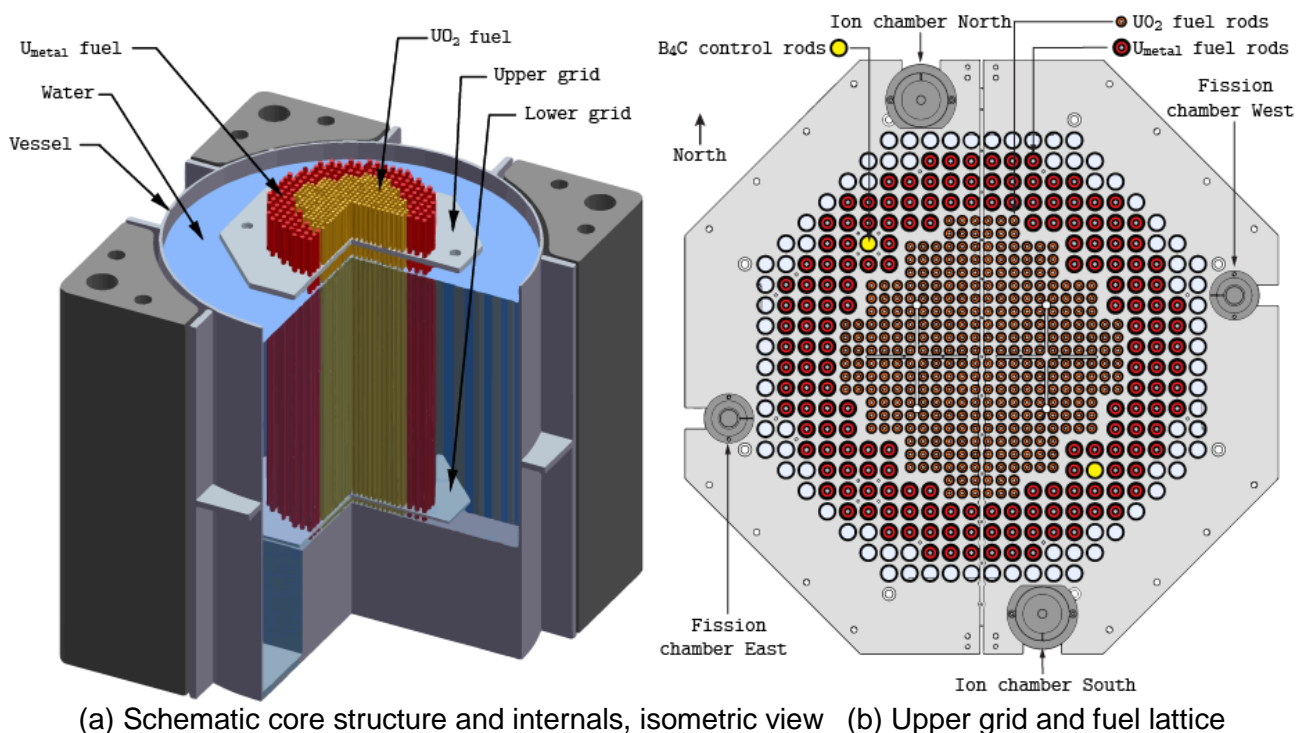
### 3 CROCUS first experimental campaign

The first experimental campaign in the CROCUS reactor took place from 17 to 21 October 2018. Vibrating fuel rods experiments were carried out using the COLIBRI in-core device (CROCUS Oscillator for Lateral Increase Between u-metal Rods and Inner zone) that was specifically developed for that purpose. This section describes the CROCUS reactor, the COLIBRI device and the vibrating fuel rods experiments.

#### 3.1 The CROCUS reactor

CROCUS is an experimental zero-power reactor, uranium-fueled and water-moderated, dedicated to teaching radiation and reactor physics, and to research. It is located at the École Polytechnique Fédérale de Lausanne (EPFL) and it has been licensed for operating at a maximum power of 100 W, i.e. a total neutron flux of  $\sim 2.5 \times 10^9$  n/cm<sup>2</sup>/s at the core center. Criticality is controlled either by changing the core's water level using a spillway, or by two B<sub>4</sub>C absorber control rods, with an accuracy of  $\pm 0.1$  mm (equivalent to approximately  $\pm 0.4$  pcm) and  $\pm 0.5$  mm, respectively. CROCUS operates at room temperature using a controlled water loop with secondary and tertiary circuits, two heat exchangers and an electrical heater.

The core is located in an aluminum vessel of 130 cm in diameter and 1.2 cm in thickness. It is filled with demineralized light water used as both moderator and reflector. Its active part has the approximate shape of a cylinder of about 60 cm in diameter and 1 m in height. It consists of two interlocked fuel zones with square lattices of different pitches: an inner zone of 336 UO<sub>2</sub> rods with an enrichment of 1.806 wt.% and a pitch of 1.837 cm; an outer zone of 172 U<sub>metal</sub> rods in nominal configuration, 0.947 wt.% and 2.917 cm; a varying water gap between the two zones because of the two different pitches. The picture of the facility and critical assembly configuration is shown on Figure 10. Both uranium fuels consist of a 1-m pile of cylindrical pellets cladded in aluminum. The rods are maintained vertically by two octagonal aluminum grid plates spaced 1 m apart. The grids have a 0.5-mm cadmium layer to limit axial neutron leakage to the environment, i.e. structures activation, with the active zone of the fuel starting above the lower cadmium layer.

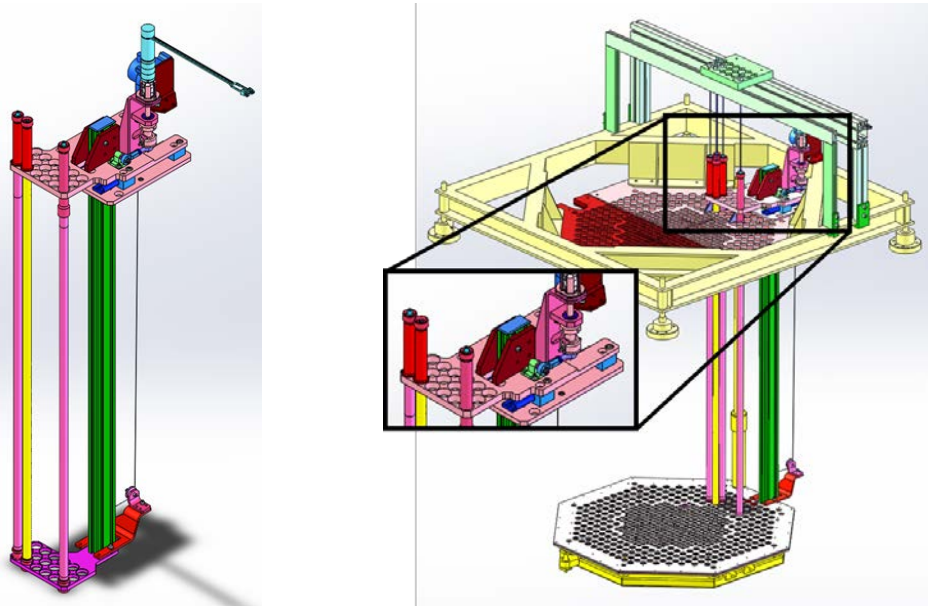


**Figure 10 – Overview of the CROCUS reactor in a reference configuration. Note: The COLIBRI fuel rods oscillation device is thus not shown.**

## 3.2 The COLIBRI experimental setup

### 3.2.1 Fuel rods oscillator

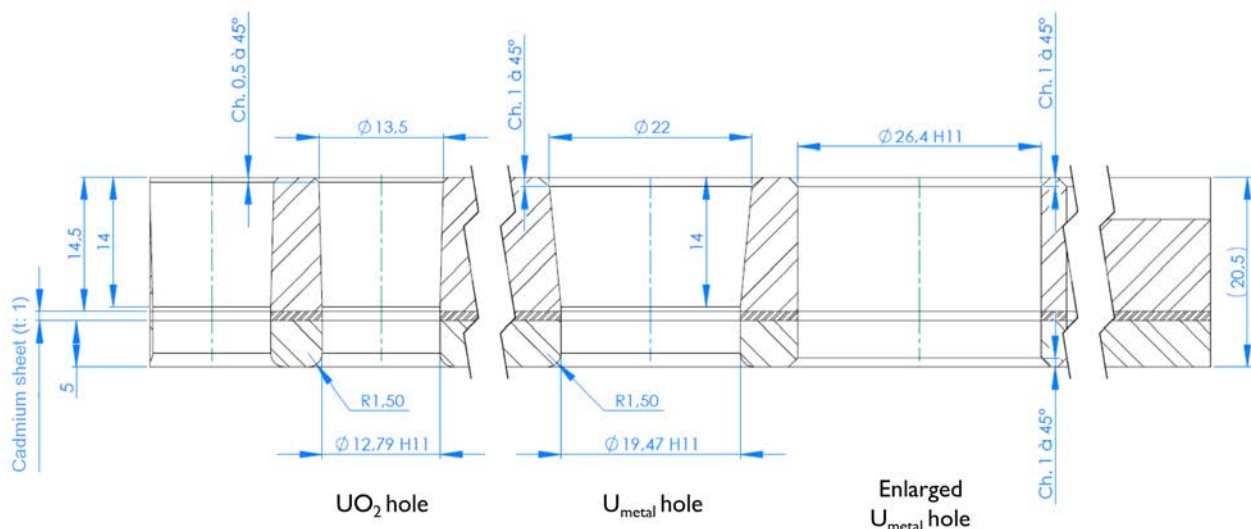
The COLIBRI fuel rods oscillator is designed to oscillate simultaneously any of 18 metallic uranium fuel rods laterally in the west region of the core periphery zone. It consists in two moving plates set above and below the core grids, and rigidly connected by an aluminum beam (see Figure 11). Each one carries an extremity of the fuel rods, top and bottom respectively.



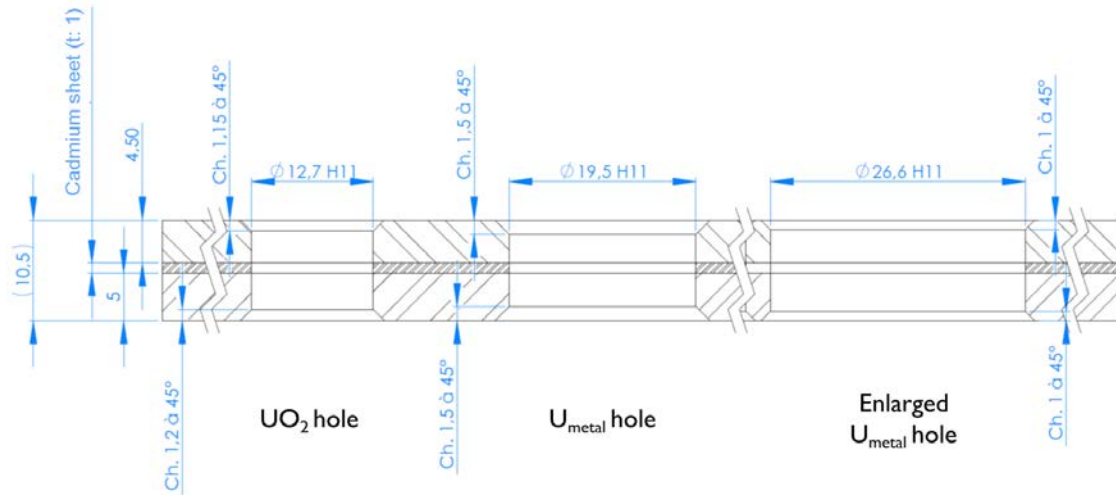
**Figure 11 – COLIBRI fuel rods oscillator alone (left) and with core structures (right), and a few rods inserted in the device.**

The top moving plate is fixed on the superior grid via gliders. Its oscillation is produced by a motor: the motor rotation is converted to a linear translation using an eccentric sheave and a rod. The oscillation is transferred to the bottom moving plate *via* the aluminum beam. The bottom moving plate is free of movement except for the connection to the transmission beam (no gliders).

New grids were produced for hosting the oscillator. Aside from the enlarged holes at COLIBRI's location, the cadmium layer set in sandwich in each grid was increased to 1-mm thickness instead of 0.5 mm. Other mechanical parts, such as those far in the reflector, or above and below the grids, are not detailed in this document as they are not relevant for the modeling.

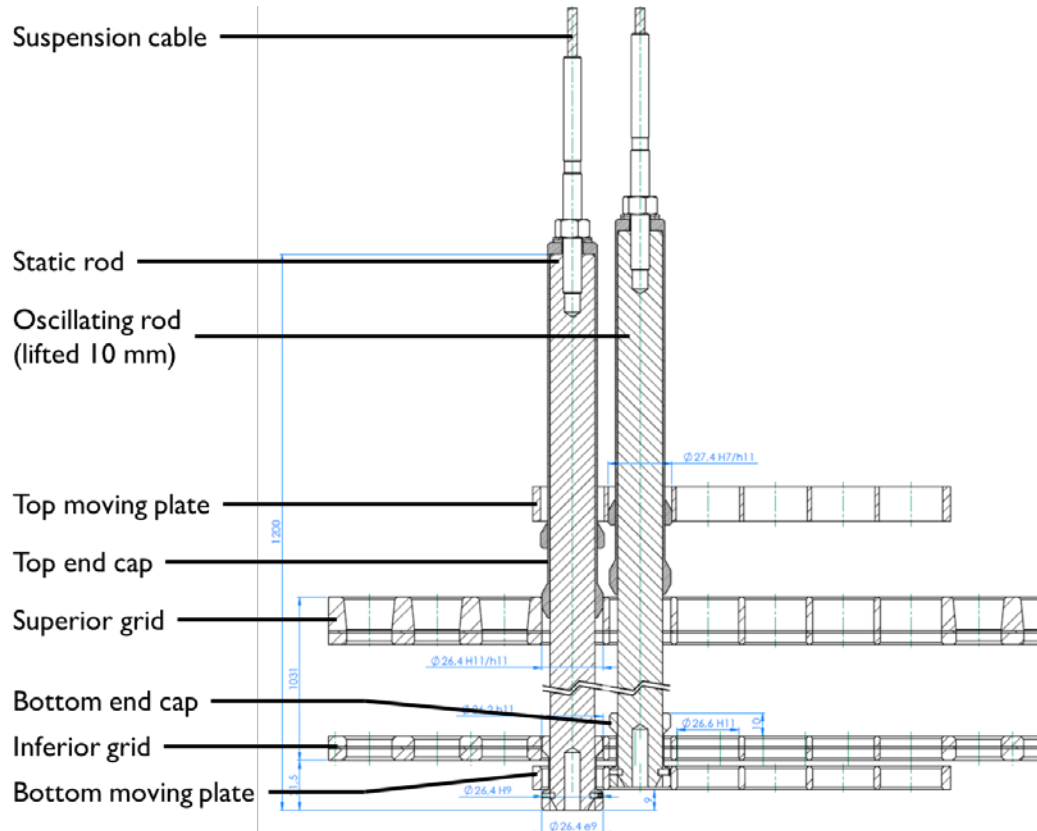


**Figure 12 – Cross section of the modified superior grid: enlarged holes in COLIBRI's region and thicker cadmium layer (1 mm).**



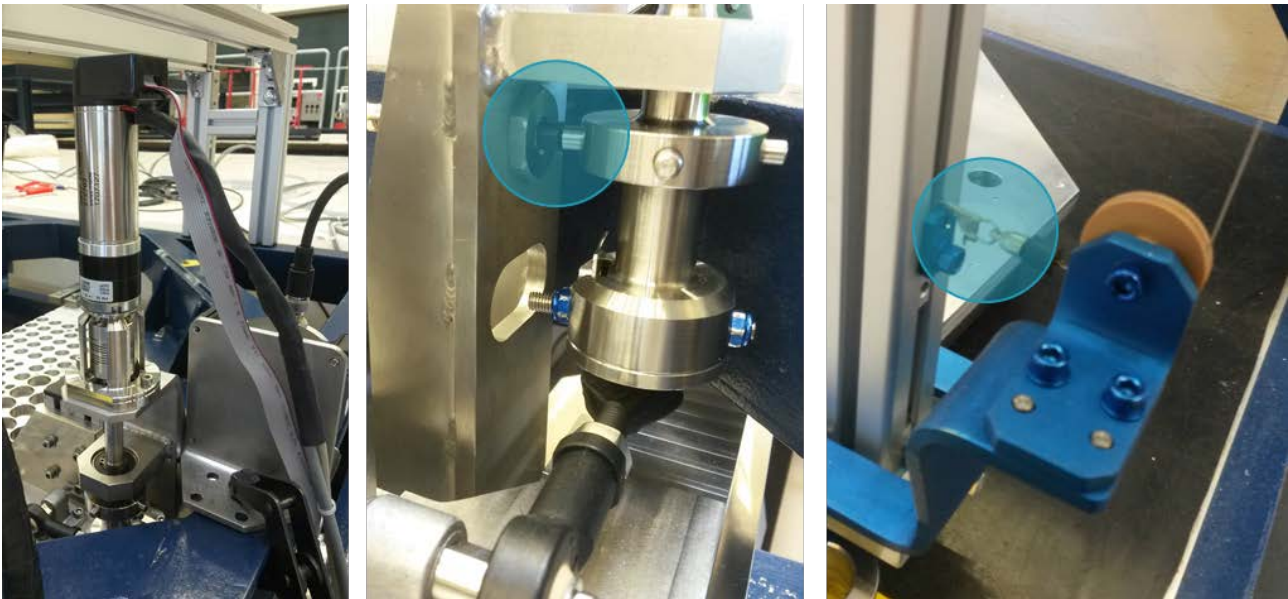
**Figure 13 – Cross section of the modified inferior grid: enlarged holes in COLIBRI's region and thicker cadmium layer (1 mm).**

The selection of the moving fuel rods is performed by leaving them laying on the reactor base plate (non-moving), or suspending them up 10 mm above the base plate to insert them in the moving plates. Top and bottom end caps are fixed to each rod to allow the insertion in the enlarged holes of either the static grids or the moving plates (see Figure 14). The weight of the oscillating rods is supported by a platform. The amplitude of the oscillation is precisely tuned by changing the eccentricity of the sheave with calibration plates, 0.5 mm by 0.5 mm from 0 to  $\pm 3$  mm in theory. Its frequency is depending on the speed of the motor, with a fixed conversion factor.



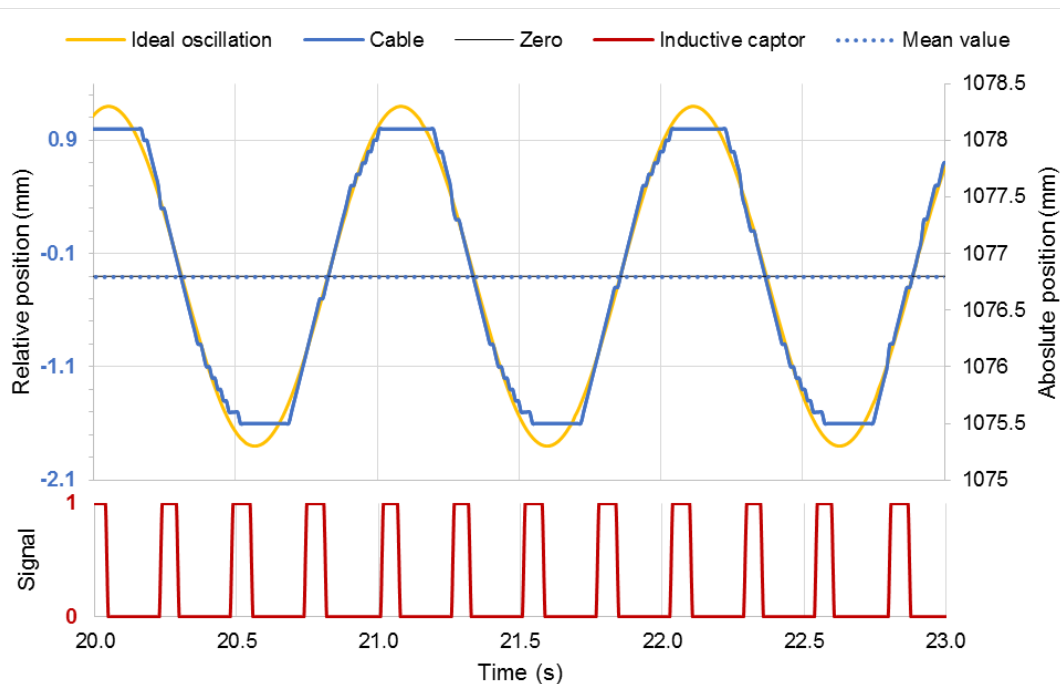
**Figure 14 – Side cross section of the oscillator with only two fuel rods inserted in it; one fuel rod is in its static configuration laying at the bottom (left), the other one is lifted up 10 mm for oscillation.**





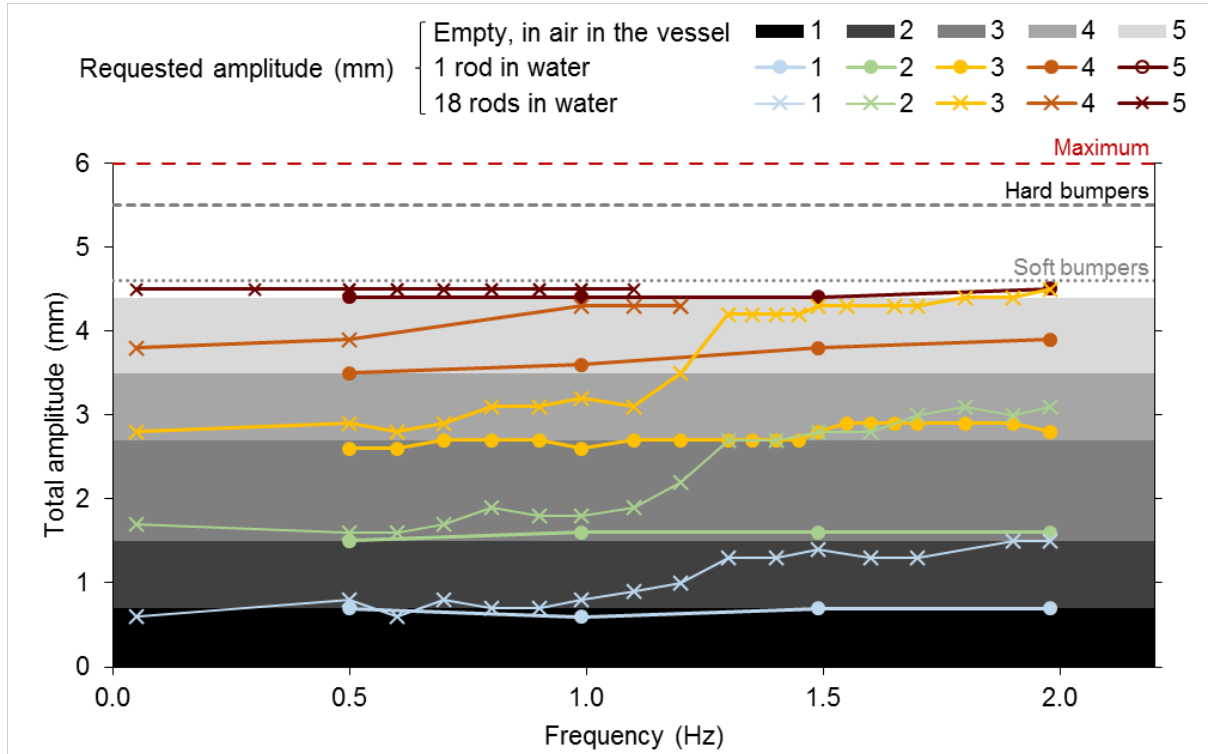
**Figure 15 – Details of the control and monitors of the oscillation: (left) Motor on its rotation axis; (center) Close-up on the rotation axis with focus (blue) on the inductive captor detecting one of the four pins; (right) Measuring cable and close-up (blue) on its connection at the bottom to the transmission aluminum beam.**

The oscillation is controlled and monitored *via* a LabVIEW-based software. An inductive captor is set at the rotation axis (i.e. at the top), which detects the actual movement of the motor by detecting the passage of four metallic pins per rotation. A cable coder is used to measure the displacement of the moving plate, i.e. at the bottom, with a 0.1 mm precision. These features are presented in Figure 15. The software provides as a csv file output the recording of the motor position and speed, the signal of the inductive captor, and the measurement of the cable, with 10 ms time-steps. A typical recording of an oscillation is presented in Figure 16. The inductive captor signal is also extracted for live and synchronized recording with the detection instrumentation.



**Figure 16 – Typical inductive captor (bottom, red) and cable (top, blue) signals, here in the case of one rod oscillating in air at  $\pm 1.5$  mm and 1 Hz. In yellow, ideal sinusoidal oscillation for comparison with the real and measured displacement.**

The behavior of the oscillator has been characterized in air and in water, out of the vessel and in-core, empty, 1-rod and 18-rods loaded. The behavior in frequency is sound. In amplitude, the device is rigid at the top, depending only on the rotation to translation conversion: a 0.1 mm flattening of the sinusoid due to plays in the crank and rod is expected (see Figure 16). The results on the oscillation amplitude at the bottom are presented in Figure 17. It demonstrates inertia effects inducing an increase of the amplitude for the full 18-rods load case and above 1 Hz, which is the case of the measurement campaign described in this report. This effect cannot be corrected, and thus has to be taken into account as is.



**Figure 17 – Comparison of the oscillator behavior at the bottom position for 1 and 18 rods loads in water (1000 mm), as compared to the device oscillating empty loaded in air (i.e. expected to be equivalent to the behavior of the top part). All measurements were carried out using the cable coder.**

### 3.2.2 Neutron detection instrumentation

The detection instrumentation comprised the facility monitors, and different types of additional ex-core and in-core detectors, for a total of eleven detectors of various sizes and sensitivities:

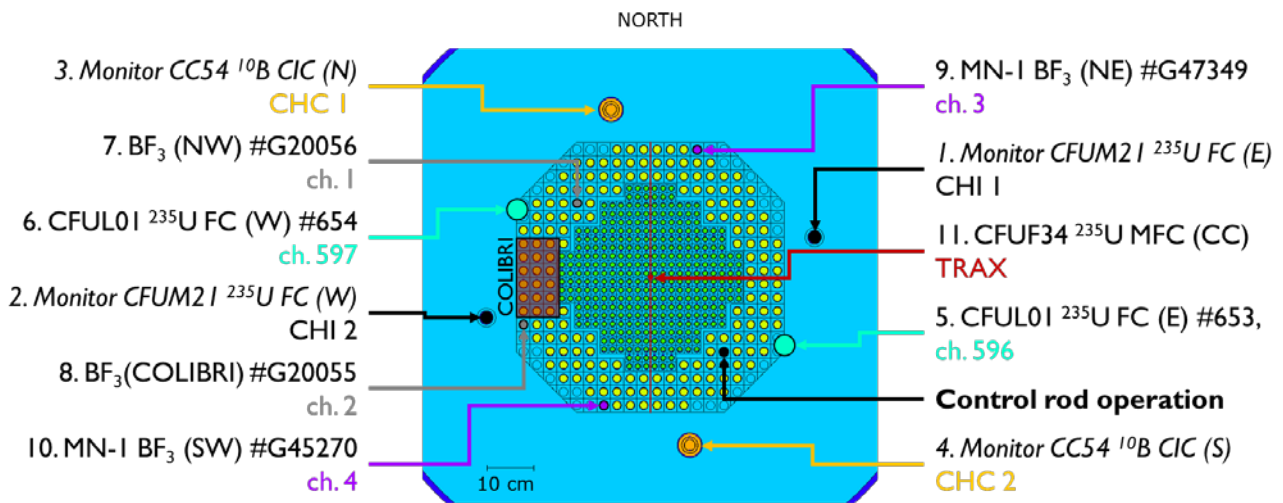
- Two operation monitors  $^{10}\text{B}$ -coated compensated ionization chambers: Merlin-Gerin CC54,
- Two safety monitors  $^{235}\text{U}$ -coated fission chambers: Photonis CFUM21,
- Two ex-core large  $^{235}\text{U}$ -coated fission chambers: Photonis CFUL01,
- Two in-core small  $\text{BF}_3$  proportional counters: Transcommerce International MN-1,
- Two in-core smaller  $\text{BF}_3$  proportional counters: unknown brand and model,
- One in-core  $^{235}\text{U}$ -coated miniature fission chamber: Photonis CFUF34.

All detectors are based on prompt detection processes. The specification and location of each of them with regards to the core and COLIBRI are presented in Table 5 and Figure 18, and with respect to the MCNP model – coordinates and universes. All four monitor detectors are set at reference positions, as presented in the CROCUS benchmark [2] and models (all available on the ECCP). The other detectors specifications, such as sensitive area and channels dimensions, are included in the Appendix 7.8. These latter were set vertically at core mid-height. On the horizontal plane, the large CFUL01 FC were set in the reflector at west (close to COLIBRI) and east positions. The  $\text{BF}_3$  counters were set at positions within the lattice as presented in Figure 18, in the control rod guide tube for the NW one (detector 3), and in aluminum channels for the others. The miniature fission chamber was set at core center. The general uncertainty on detector position is  $\pm 1$  mm.

**Table 5 – Detectors specifications and locations with respect to the MCNP model coordinates. In italic, location coordinates within the lattice.**

Detector								Location		
#	Type	Brand	Model	Number	Instrum. Channel	Sensitive material	Approximate sensitivity	E	N	MCNP
1	FC	Photonis	CFUM21	-	CHI 1	<sup>235</sup> U coating	10 <sup>-2</sup> n <sub>th</sub> <sup>-1</sup>	+35.8	+8.7	u = 31
2	FC	Photonis	CFUM21	-	CHI 2	<sup>235</sup> U coating	10 <sup>-2</sup> n <sub>th</sub> <sup>-1</sup>	-35.8	-8.7	u = 31
3	CIC	Merlin-Gerin	CC54	-	CHC 1	<sup>10</sup> B coating	3×10 <sup>-14</sup> A.n <sub>th</sub> <sup>-1</sup>	-8.6	+36.35	u = 30
4	CIC	Merlin-Gerin	CC54	-	CHC 2	<sup>10</sup> B coating	3×10 <sup>-14</sup> A.n <sub>th</sub> <sup>-1</sup>	+8.6	-36.35	u = 30
5	FC	Photonis	CFUL01	653	596	<sup>235</sup> U coating	1 n <sub>th</sub> <sup>-1</sup>	-29.8	+15.4	-
6	FC	Photonis	CFUL01	654	597	<sup>235</sup> U coating	1 n <sub>th</sub> <sup>-1</sup>	+29.8	-14.7	-
7	PC	-	-	G20056	1	<sup>10</sup> BF <sub>3</sub> gas	10 <sup>-2</sup> n <sub>th</sub> <sup>-1</sup>	-16.0435	16.0435	-
8	PC	-	-	G20055	2	<sup>10</sup> BF <sub>3</sub> gas	10 <sup>-2</sup> n <sub>th</sub> <sup>-1</sup>	-27.7115	-10.2095	-
9	PC	Trans. Int.	MN-1	G47349	3	<sup>10</sup> BF <sub>3</sub> gas	10 <sup>-2</sup> n <sub>th</sub> <sup>-1</sup>	10.2095	27.7115	u = 21
10	PC	Trans. Int.	MN-1	G45270	4	<sup>10</sup> BF <sub>3</sub> gas	10 <sup>-2</sup> n <sub>th</sub> <sup>-1</sup>	-10.2095	-27.7115	u = 21
11	MFC	Photonis	CFUF34	-	TRAX	<sup>235</sup> U coating	10 <sup>-3</sup> n <sub>th</sub> <sup>-1</sup>	0	0	-

The operation ionization chambers and the large fission chambers were operated in current mode, whereas all the other detectors were operated in pulse mode. The detectors and their electronics were connected to the ISTec, TUD, and both EPFL pulse and current mode instrumentations as presented in Appendix 7.7 (p. 48), with a number of detectors depending on the number of possible inputs. In addition, the safety monitors were used in MCS mode for power monitoring.



**Figure 18 – Experimental locations of detectors, with their ID, details and instrumentation channel.**

### 3.3 Measurements

Two types of measurements were carried out: static, and a range of measurements in oscillation. The reactor was operated with the south control rod (see Figure 18), at a fixed water level of  $1000 \pm 0.1$  mm. Following linearity tests, the power was set around 100 mW, and the water temperature was controlled at  $20.0 \pm 0.1$  °C. In all cases, the 18 rods were lifted in the oscillation position: in the static case, the motor was off and the position was set at zero (i.e. in their normal position within the lattice). The global reactivity effect of the oscillations was compensated to follow a stable power. In practice, the oscillation was started first, then the reactor was stabilized in power with the control rod before starting the measurement. The control rod insertion was updated along the operation and measurement.



### 3.3.1 Measurements list

The whole list of measurements is presented in Table 6 below with their identification number. 20 measurements were carried out in total, with little redundancy, and mainly to compensate early stage mistakes or issues. All measurements were acquired by all three systems. The duration of each measurement was chosen to cover enough cycles of the perturbation oscillation (around 1000, except for 0.1 Hz). In addition, a minimum of one half-hour is required to obtain a stable zero-power noise PSD with the majority of the detectors. As a consequence, the minimum half-hour duration was extended to one hour for the lower perturbation frequencies (0.1 and 0.5 Hz). Table 6 includes the oscillation specifications as well as the final control rod position, and water level oscillation. Indeed, waves at the surface induced by oscillations were measured using the reactor instrumentation (INUS ultrasonic sensor). The indicated values correspond to the maximum range observed. Turning back to the fuel rods, the oscillation is described in displacement amplitude and frequency, with a difference between requested and measured ones. The difference in amplitude is explained in the previous section (3.2.1). As a consequence two types of oscillation time series will be distributed: one file per amplitude for top displacement, and one for each measurement for the bottom. The frequency difference is due to a fixed conversion factor between software motor speed and real frequency (unknown during the campaign): the measured value is the true one. In addition to the detailed measurements list with all specifications, for each measurement the following will be provided in the form of time series:

- the detectors' signals available from each detection instrumentation,
- the inductive captor output recorded by ISTec acquisition system,
- the oscillator's output for each corresponding oscillation (motor, inductive captor, cable),
- the two power monitors outputs.

**Table 6 – Measurements list with corresponding reactor state (including final position of control rod, and water level oscillations' amplitude), and oscillation specifications (amplitude, frequency, and ID).**

Measurement				Reactor			Oscillation					
#	Date	Start	Duration	Power	Control rod	Water osc.	Amplitude		Frequency		Osc. ID	
							Req.	Meas.	Req.	Meas.		
			min	mW	mm	mm	mm		Hz		-	
1	18.09.18	12:38	variable	100	180	-	static					
2	18.09.18	16:10	15	110	189		±1.5	3.2	1.0	0.972	386_1,5_22	
3	18.09.18	16:36	30	110	189		±1.5	3.2	1.0	0.972	386_1,5_22	
4	19.09.18	09:46	30	100	186		±1.5	3.0	0.5	0.486	387_1,5_11	
5	19.09.18	10:44	30	100	182	0.8	±1.5	4.2	1.5	1.458	389_1,5_33	
6	19.09.18	11:34	30	100	178	0.2	±1.5	4.5	2.0	1.944	391_1,5_44	
7	19.09.18	12:28	60	100	170	0.1	±1.5	2.8	0.1	0.097	393_1,5_2,2	
8	19.09.18	16:04	30	100	176	0.1	±0.5	0.7	0.5	0.486	396_0,5_11	
9	19.09.18	17:10	30	100	178	0.1	±0.5	0.7	1.0	0.972	397_0,5_22	
10	19.09.18	17:52	60	100	178	0.1	±0.5	0.7	0.1	0.097	398_0,5_2,2	
11	20.09.18	09:15	30	100	188	0.1	±2.0	3.8	0.5	0.486	400_2_11	
12	20.09.18	10:42	60	100	184	0.1	±2.0	3.7	0.1	0.097	401_2_2,2	
13	20.09.18	12:04	30	100	188	0.3	±2.0	4.0	1.0	0.972	403_2_22	
14	20.09.18	14:14	30	100	180	0.2	±1.0	1.7	0.5	0.486	405_1_11	
15	20.09.18	15:05	60	100	180	0.1	±1.0	1.7	0.1	0.097	406_1_2,2	
16	20.09.18	16:21	30	100	180	0.2	±1.0	1.8	1.0	0.972	407_1_22	
17	20.09.18	17:09	30	100	180	0.6	±1.0	2.7	1.5	1.458	409_1_33	
18	20.09.18	17:49	30	100	174	0.6	±1.0	3.3	2.0	1.944	411_1_44	
19	21.09.18	09:03	60	100	180	0.0	±1.5	2.8	0.1	0.097	412_1,5_2,2	
20	21.09.18	10:21	120	100	183	0.2	±1.5	3.2	1.0	0.972	413_1,5_22	

### 3.3.2 Uncertainties in measurements

The identified uncertainties list as follows:

- Reactor operation:
  - o water level:  $\pm 0.1$  mm
  - o control rod insertion:  $\pm 0.5$  mm
  - o temperature:  $0.1$  °C (conservative)
  - o power: 5% in absolute (uncertainty of power calibration with gold foils activation), time evolution described in relative by the safety monitors (counts per second in time series to be provided, i.e. statistical)
- Oscillator:
  - o top position:  $\pm 0.1$  mm (conservative)
  - o bottom position:  $\pm 0.1$  mm (cable precision)
  - o time resolution: 10 ms
  - o frequency:  $\pm 0.01$  Hz (conservative)
- Detection:
  - o detectors location:  $\pm 1$  mm
  - o signal: statistical for counts, to be extracted from the raw data more generally.

## 4 Qualification of data acquisition systems

As outcome of the subtask 2.1.1, in the following part are described the EPFL, TUD and ISTec acquisition systems. EPFL and TUD acquisition systems are then compared against the industry-grade ISTec system for qualification purposes, based on the measurements of the AKR-2 campaign.

### 4.1 Description of the acquisition systems

#### 4.1.1 ISTec data acquisition system: SIGMA

The ISTec data acquisition (DAQ) system, named SIGMA, is highly specialized in measuring noise signals coming from neutron flux density fluctuations. These signal fluctuations contain the information about the reactor state and behavior: they are correlated to the general statistical behavior of fission processes, and fluctuations of reactor core internals (e.g. pressure, flow, etc.). These phenomena create stochastic and deterministic perturbations of local or global neutron flux, i.e. neutron noise signals. In general, the noise is very small and has amplitudes of some percent of the whole signal only. The neutron flux signals show additionally a decrease of noise amplitudes for higher noise frequencies. For instance, there is a decrease of more than six decades in the frequency range up to 20 Hz in PWRs.

SIGMA measures voltage signals with an amplitude range of  $\pm 10$  V provided by in core or ex-core neutron detectors. Depending on detector type and counting rate, the original pulse or current signals are converted to voltage signals by detector specific preamplifiers, and in the case of pulse signals by an additional frequency-to-voltage-converter (integrating counter system) to transform pulses into voltage fluctuations. Absolute signals correlated to neutron flux are treated in order to strip the constant signal contribution (DC-part, representing the average neutron flux) from the fluctuating signal fractions of interest (AC-part). In order to get a high resolution in the analogue to digital conversion, the signals are compensated for the DC-part and amplified for the AC-part. The compensation of the DC-part of a signal by a fixed DC-value has no influence on the signal in contrast to a high-pass filtering. The fixed DC-value is determined prior to the measurement and fixed during the acquisition. It is based on the short-time mean value of the signal. The residual AC-part or fluctuating signal will be amplified, filtered to cut higher frequent contributions, and finally sampled to digital signals for recording. The signals are then post-processed to recalculate the fluctuation using the applied gain, allowing the subsequent frequency analysis, e.g. Fast Fourier Transform (FFT). In order to identify noise signals with small amplitudes, i.e. respectively small contribution to the total detector signal, the system is optimized with regards to very low interfering intrinsic electronic noise level. The system is illustrated in Figure 19.

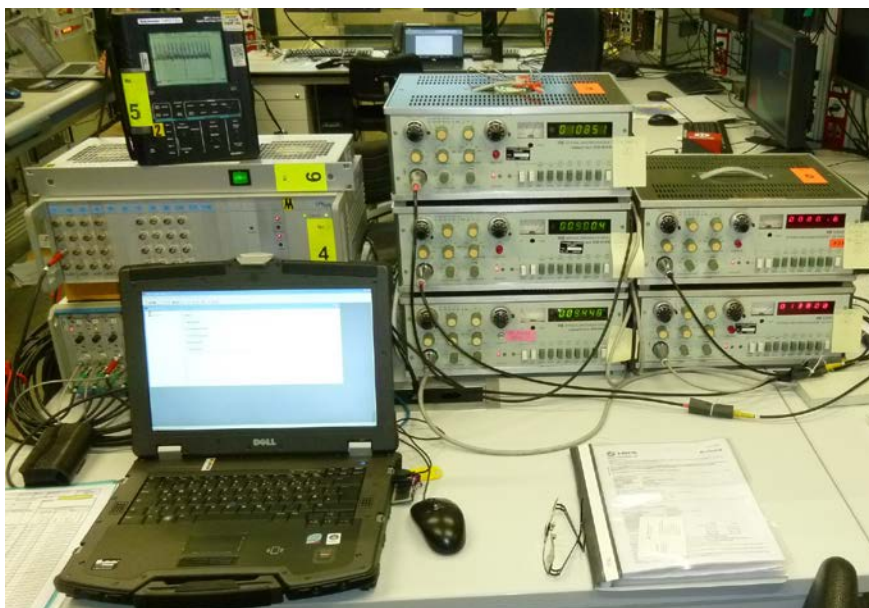


Figure 19 – ISTec SIGMA data acquisition system (left) connected to five ROBOTRON units (right).

The signal treatment comprises a stepwise processing listed below:

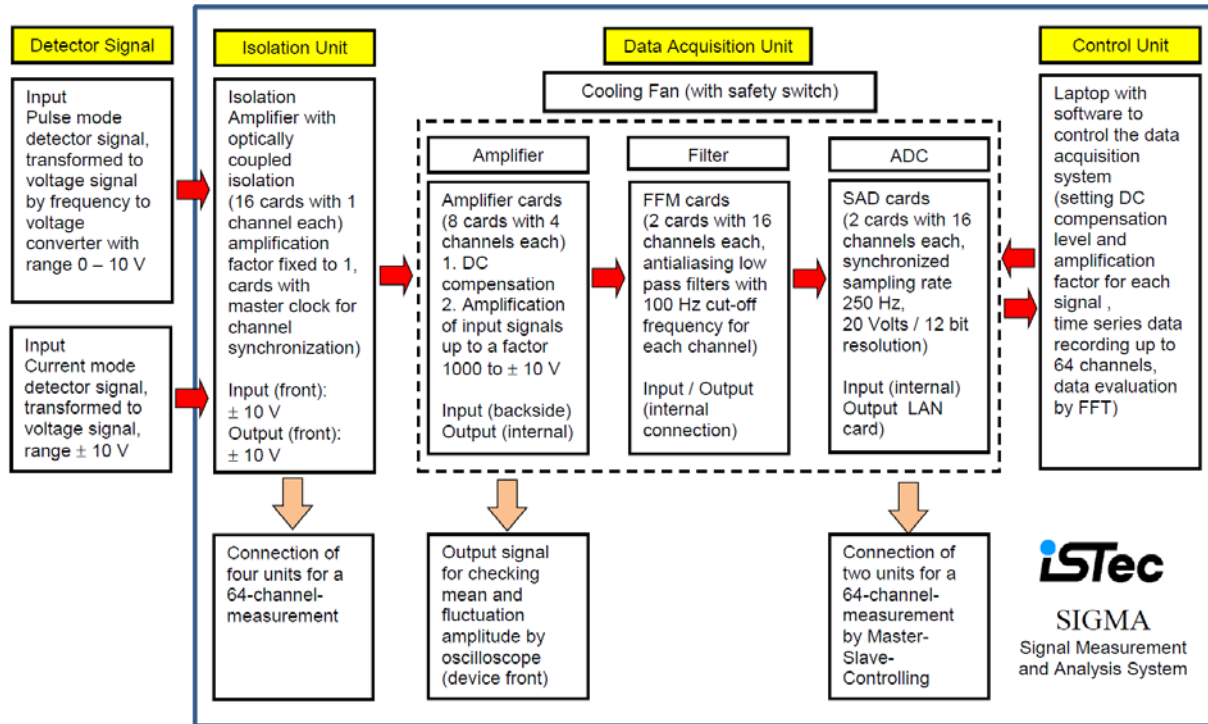
- *1<sup>st</sup> step:* Galvanic isolation of input voltage signals from electronics of the detector system by isolation amplifiers.
- *2<sup>nd</sup> step:* Compensation of constant fraction of the detector signal by application of a constant voltage signal with opposite polarity (DC compensation) by low noise AMP card (Amplifier Module).
- *3<sup>rd</sup> step:* Amplification of the residual fluctuating signal fraction (maximum amplification factor: 1000, maximum output signal:  $\pm 10$  V). Because of the special low noise design of the amplifiers, no significant artificial signals are created by the amplification process. Therefore no discrimination of the resulting signal against background is needed.
- *4<sup>th</sup> step:* Separation of residual fluctuating voltage signal from contributions with higher frequencies by anti-aliasing low pass filter for each channel by a FFM card (Fix Filter Module), with 100 Hz cutting frequency limit according to the frequency limit for subsequent signal sampling at 250 Hz (Nyquist frequency about 125 Hz). The low-pass cut-off frequency has to be less than half of the sampling frequency to avoid antialiasing effects.
- *5<sup>th</sup> step:* Sampling of residual fluctuating voltage signal at 250 Hz and 12 bit resolution covering a range of 20V simultaneously for 16 channels by SAD card (simultaneous analog-digital converter) creating digital voltage signals closely reflecting fluctuation of respective original detector signals.

These steps are implemented in a setup of successive units which are presented below and illustrated in Figure 20:

- *Pulse convertor:* for detector signals not fitting the input conditions of the system (e.g. pulse signal for individual neutron detections) additional electronics is needed for signal transformation. A proven method comprises the application of a frequency-to-voltage converter (e.g. ROBOTRON 20046). Such a system measures pulse signals period (no pulse shape integration) for a given time (e.g. 4 ms) and creates a proportional voltage output signal. As for any other pulse mode detection system, it requires a discrimination of pulses correlated to neutron flux from background signals (e.g. electronics noise). This module is not part of SIGMA, but used at the front-end.
- *Isolation Unit:* voltage signals from the detectors are applied as input to the optical isolation amplifier (Imtron ISO-DP). The main task of this part is to galvanically decouple the subsequent system from the electronics of the detection system, in order to avoid trouble coming from differences at equipotential bonding, or feedback to the detector system. While called “amplifier”, no amplification (amplification factor = 1) or other signal modification is performed in this stage. The input signal is limited to a range of  $\pm 10$  V and below a frequency of 20 kHz. Each detector signal is handled by a separate isolation amplifier. ISTec has different racks with 8 and 16 isolation amplifiers.
- *Data acquisition unit:* the data acquisition rack contains three types of cards to allow time-synchronized processing of 32 detector signals transferred from the isolation unit output. Cards are separated in two sets each covering 16 detector channels. Each set consists of 4 amplifier cards with 4 amplifiers each, an anti-aliasing low pass filter card (FFM card) consisting in 16 separate filters, and finally an analog-digital converter card consisting of 16 separate simultaneously operating 12 bit AD-converters (SAD card). In total 32 signals can be measured by one rack. A second rack equipped with the same set of cards can be connected by a LAN-based master-slave interface extending number of channels simultaneously operated by additionally 32 channels. For checking the zero point level of the fluctuating detector signal after DC compensation and amplification, each amplifier card is equipped with front connectors for each amplifier channel, providing separate output signal for manual evaluation of the fluctuating signal shape and position by oscilloscope.
- *Control unit:* SIGMA runs with a specifically developed software managing not only DC compensation for the original detector signal, setting of zero point level for each detector signal and adjustment of amplification factor (typical amplification range 20 to 40) of resulting

fluctuating signal (see low noise amplifier card), but also recording the finally sampled digital data out of SAD card on a hard disk drive ready for further analysis (e.g. FFT). This software also allows a rough preliminary analysis to check the data quality but it is not intended for a detailed data analysis.

All electronics are kept at constant temperature condition by a cooling fan.



**Figure 20 – Measurement scheme of ISTec DAQ SIGMA.**

To get most benefit from sampling and conversion, the fluctuating signals need to be amplified in a way to cover most of the given SAD resolution range of 20 V. On the other hand, sticking with the amplification factor close to the resolution range limit may cause problems during the measurement if the detector signal is spiking or shifting (e.g. by varying reactor power level) in a way that it exceeds the adjusted amplification range. Beside the technical setup of the data acquisition system, this adjustment of individual amplification factors for each detector signal is the base for satisfactory measurement results, and it needs good experience in neutron flux measurement and performance of the individual specific detectors. Judgment on appropriate amplification factors in advance of real measurement behavior of each detector signal will be individually evaluated for a certain time period.

#### 4.1.2 EPFL acquisition systems

EPFL uses two types of instrumentations for noise measurements: one operated in pulse mode, and one operated in current mode.

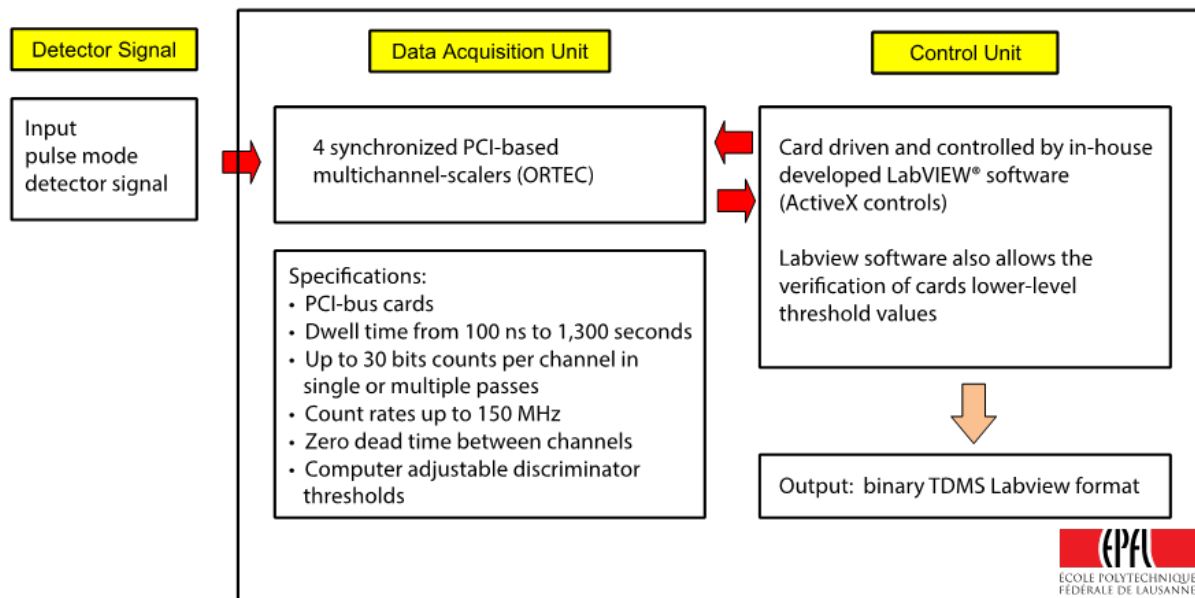
##### 4.1.2.1 Pulse mode acquisition system

The EPFL pulse acquisition system (see Figure 21) comprises four synchronized PCI-based multichannel-scalers (from ORTEC) which have the ability to store up to 65K data points and sample at a maximum of 150 MHz. The acquisition is controlled by LabVIEW routines. This system was used to record the signals from the pulse mode detectors during both AKR-2 (detectors 1 to 4) and CROCUS (detectors 7 to 10) measurement campaigns. Because the start of the acquisition by a trigger signal is not implemented in the LabVIEW routines, the fourth PCI-card was temporally unplugged from its detector at the start of the measurements to record the signal of the TTL trigger. This allowed the time series synchronization during data post-processing. The measurement scheme is depicted in Figure 22.





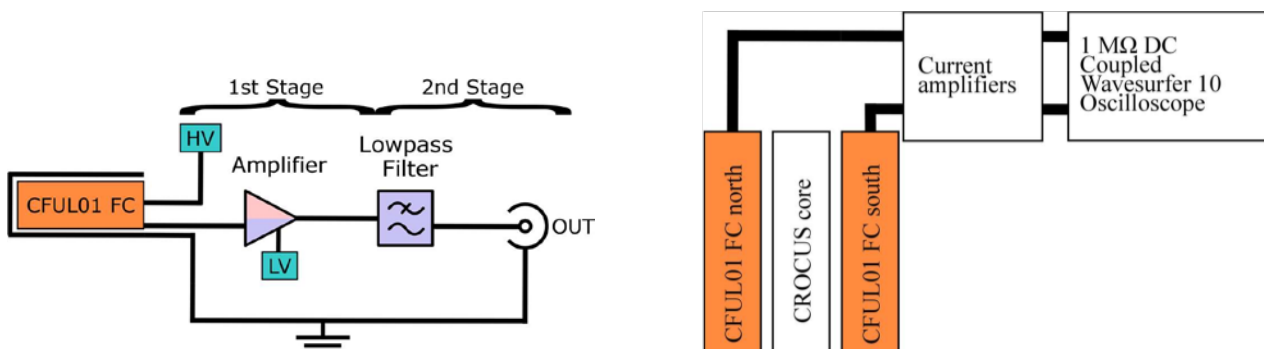
**Figure 21 – EPFL data acquisition system.**



**Figure 22 – Measurement scheme of EPFL/PSI pulse mode acquisition system.**

#### 4.1.2.2 Current mode acquisition system

In addition to the pulse mode acquisition system described above, EPFL uses a current mode acquisition system consisting in a Lecroy Wavesurfer 10 oscilloscope. This system was used to record the signals from the current mode detectors during the CROCUS (detectors 3 to 6) measurement campaign. Amplification and measurement schemes are depicted in Figure 23.



**Figure 23 – On the left, schematic of the in-house developed current amplifier connected to a typical large FC Photonis CFUL01, such as those used during the CROCUS campaign (detectors 5 and 6); on the right, schematic of the instrumentation channels connected to the oscilloscope used as acquisition system for current mode measurements.**

#### 4.1.3 TU Dresden acquisition system

TU Dresden acquisition system is similar to that one from EPFL (ORTEC MCS-pci) except that it uses a single PCI-card and is based on the ORTEC acquisition software (MAESTRO). This system was used to record the signal from detector 1. The external TTL signal was used to trigger the acquisition. The measurement scheme is depicted in Figure 24.

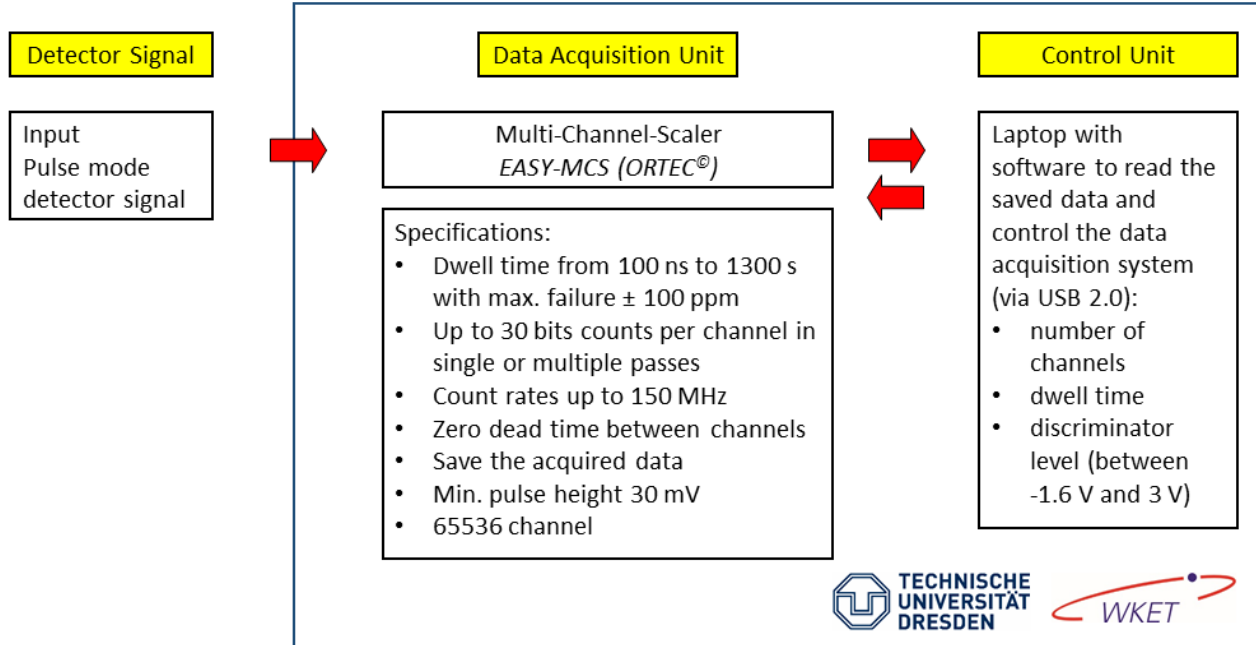


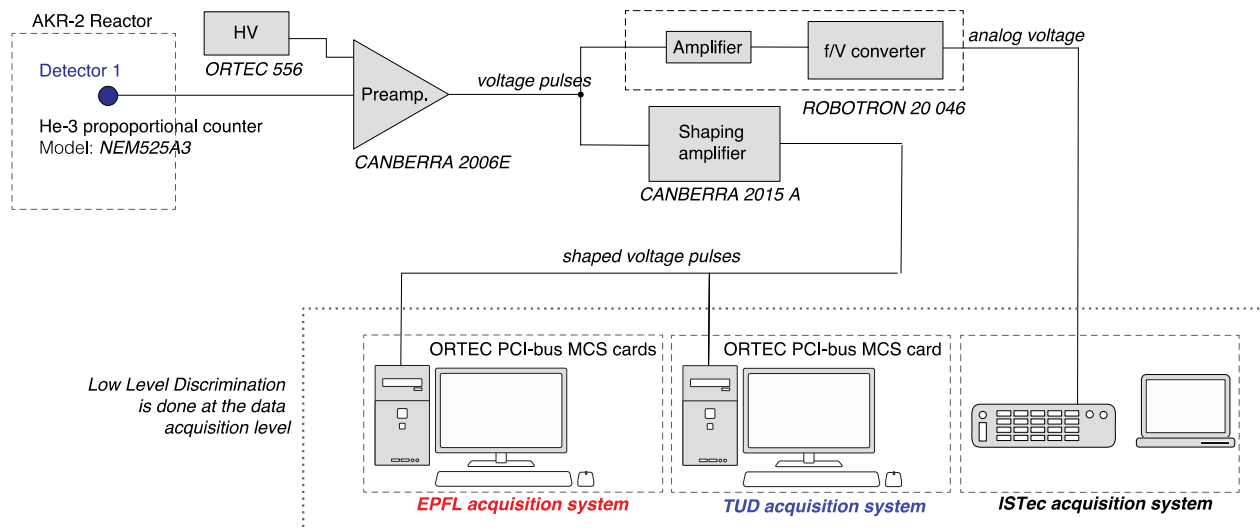
Figure 24 – Measurement scheme of TUD acquisition system.



## 4.2 Benchmarking and qualification of data acquisition systems

The performance of TUD and EPFL data acquisition systems were benchmarked against the one from ISTec, named SIGMA. The latter has been chosen as the reference for the benchmark as it provides the quality suitable for industrial use.

### 4.2.1 Benchmark description



**Figure 25 – AKR-2 detection chain for DAQ benchmarking.**

The benchmarking focuses on the frequency analysis of data acquired in the first AKR-2 campaign (Section 2.3), and the data of one measurement acquired during the first CROCUS campaign (Section 3.3). A total of twenty-eight measurements were used for the benchmarking: ten corresponding to the rotating absorber experiments, seventeen to the vibrating absorber experiments, and one to the vibrating fuel rods experiments. The lists and details of these experiments is shown in Table 3, Table 4, and Table 6. The comparison between the three DAQs is possible for signals from detector 1 (see Table 2) in the AKR-2 campaign, because the TUD system recorded data for this detector only. The detection chain used for this benchmarking is shown in Figure 25. For the CROCUS campaign, the comparison was only possible for the experiment 3, using the signal from detector 8 (see Table 5 and Figure 18). Note that the electronics associated with the detection are not the same for ISTec as for EPFL and TUD acquisition systems because the required input signals are different. The different electronics may have an impact in the comparison. Furthermore, even for the TUD and EPFL cases where the associated electronics are the same, each data acquisition system (DAQ) set up a specific lower level discrimination. An additional comparison focuses on a detector operated in current mode (detector 6), in order to directly compare ISTec SIGMA, without ROBOTRON, with the EPFL current mode system. The TUD pulse mode system is incompatible with such type of signal.

The main peak amplitude (corresponding to the fundamental frequency) of the power density spectrum is an indicator of how much weight this frequency will contribute to the overall signal power, and thus was chosen as the parameter for the comparison of data acquisition systems. Because the signals are subjected to various sources of noise that are distributed throughout the frequency spectrum, the comparison in terms of peak amplitudes is meaningful.

Prior to computing the peak amplitudes, several steps need to be taken to post-process the signals obtained from the three data acquisition systems. The step-by-step procedure is described below in this section. The scripts used for the data post-processing were written in the Python language and are provided in Appendix 7.9.

The first step consists in synchronizing the three signals in time to ensure that the comparison is carried out for the same time interval. This required to use the trigger signal recorded by ISTec and EPFL systems to assign a zero reference in the time domain. No treatment is required to synchronize TUD data because their DAQ was automatically launched by the same trigger signal measured by the other two DAQs.

Because the detectors' signals are processed differently according to each DAQ, the second step is to standardize the data prior to any treatment in the frequency domain. The data standardization is a straightforward procedure that starts by subtracting the mean value of the signal (time series), resulting in a mean of zero. Then, the resulting zero-mean signal is divided by the standard deviation, which results in a time series with standard deviation of one. The process is expressed by the following equation:

$$(1) \quad X_{std} = \frac{X - \bar{X}}{\sigma_X}$$

where  $\bar{X}$  and  $\sigma_X$  are the mean value and the standard deviation of the time series signal  $X$ , respectively.  $X_{std}$  is the standardized time series.

The following step is to compute the power spectral density (PSD). For simplicity reasons, the periodogram method was used for the PSD estimation. The one side PSD is given by:

$$(2) \quad P_{XX} = \frac{2|FFT(X)|^2}{f_s N}$$

where  $FFT(X)$  is the Fast Fourier Transform of the signal  $X$ ,  $f_s$  is the signal sampling frequency and  $N$  the number of signal data points.

The frequency is an array of size  $N/2$  that goes from zero to  $f_s/2$ , with a frequency resolution of:

$$(3) \quad \Delta f = \frac{f_s}{N}$$

Finally, the amplitude of the peak corresponding to the fundamental frequency was found by searching for the maximum peak value in the power density spectrum for frequencies larger than 0.1 Hz. The cutoff frequency of 0.1 Hz was set because in some cases the amplitude at lower frequencies exceeds that one of the main peak.

#### 4.2.2 Uncertainty quantification on peak amplitude estimate

The signals acquired during the experimental campaigns carry information from two main sources of fluctuations. The first fluctuation source results from the induced perturbation and thus is the one of interest for its accurate identification. The induced perturbation fluctuations will be hereafter referred to as 'signal'. The second fluctuation source is given by the inherent randomness of the neutron chain. Because these fluctuations are practically random and contain no useful information for this analysis, they will be referred to as 'unwanted noise'. An additional source of unwanted noise may arise from the detection systems electronics.

The estimation of parameters from the power density spectrum is subjected to uncertainties related to the acquisition time and the unwanted noise (i.e. random fluctuations). A small reactivity perturbation in the reactor will result in a time series with low signal-to-(unwanted) noise ratio and thus, resolving the fundamental frequencies will require longer acquisition times than the large

perturbation counterpart. Because the uncertainties are related to the signal's unwanted noise, for a fixed time length, the uncertainties are expected to be higher in the case of small perturbations.

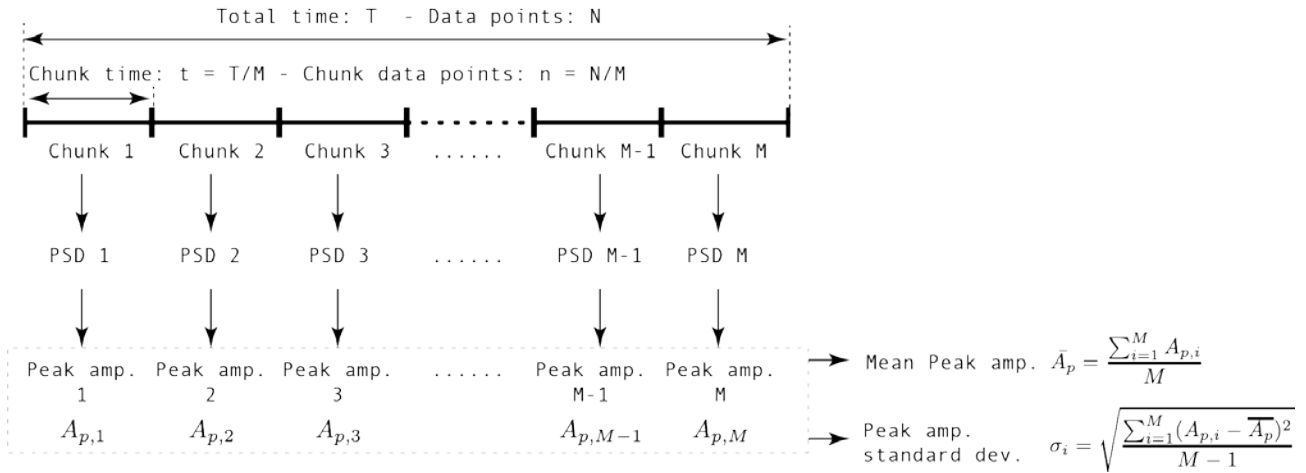
The present section shows the method for quantifying the uncertainty associated to the length of the signal. Note that this uncertainty decreases with the acquisition length and approach zero in the ideal case where the acquisition length tends to infinite.

The process for quantifying the uncertainty is schematized in Figure 24 and relies on slicing the signal (from any DAQ) in M smaller chunks. Next, the PSD for each chunk is estimated using the method described above, and each PSD is later used to compute M peak amplitudes. The sampled peak amplitudes are then used to compute the mean peak amplitude, which is given by:

$$(4) \quad \bar{A}_p = \frac{\sum_{i=1}^M A_{p,i}}{M}$$

The standard deviation of each chunk sample is computed as:

$$(5) \quad \sigma_i = \sqrt{\frac{\sum_{i=1}^M (A_{p,i} - \bar{A}_p)^2}{M-1}}$$



**Figure 26 – Uncertainty quantification process for peak power estimation.**

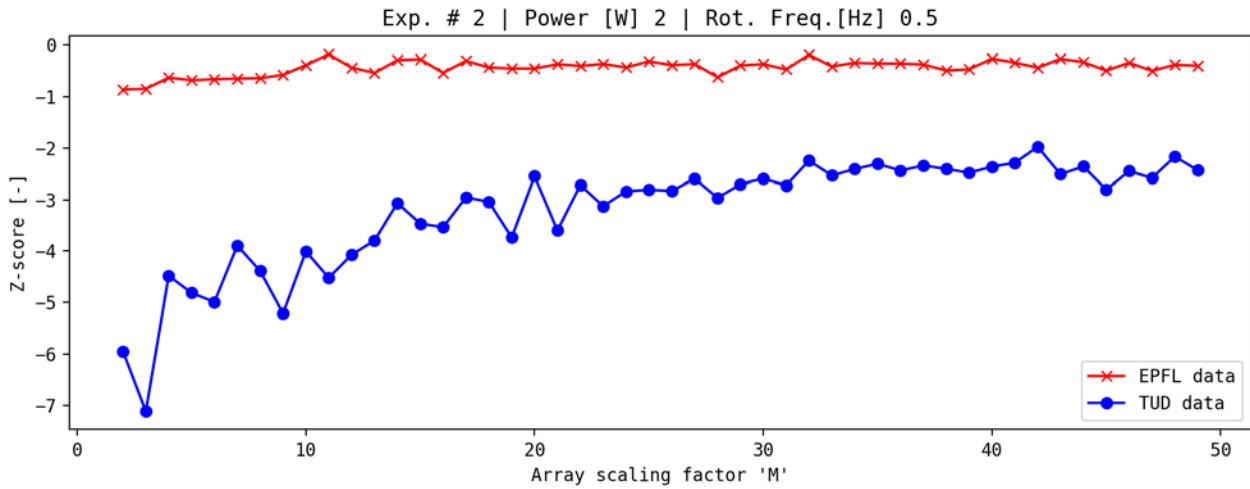
The figure of merit for evaluating benchmark results is the z-score defined as:

$$(6) \quad z = \frac{\bar{A}_{p,x} - \bar{A}_{p,ISTec}}{\sqrt{(\sigma_{i,x})^2 + (\sigma_{i,ISTec})^2}}$$

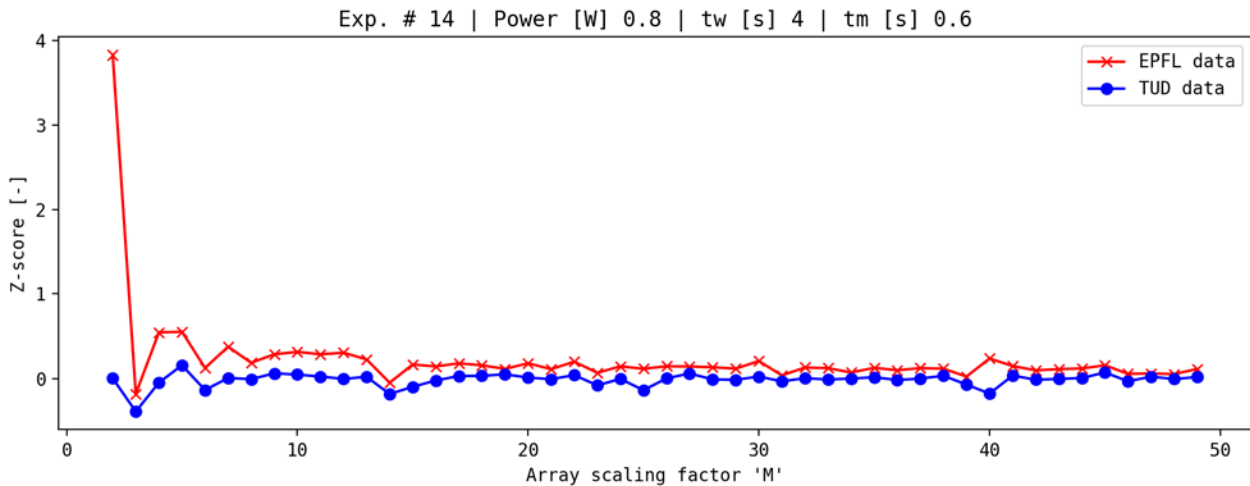
where  $\bar{A}_{p,x}$  and  $\sigma_{i,x}$  are the mean peak amplitude and standard deviation from EPFL (or TUD) data, respectively given by equations (4) and (5).

It is worth noting that the scaling factor M should not be arbitrarily chosen. A very small M factor provides good estimation of each individual chunk peak amplitude ( $A_{p,i}$ ), but a small sample size for estimating the standard deviation ( $\sigma_i$ ). On the other hand, a large M factor provides good statistics for the standard deviation, but a low frequency resolution ( $\Delta f = \frac{M f_s}{N}$ ) and thus a weaker estimate of the peak amplitude. An investigation of the impact of the choice of M over the z-scores has been performed to show that the benchmarking results shown below (computed with a fixed M value) do remain confined after certain value of M. Figure 27 and Figure 28 show the z-score as a function of M for the rotating absorber and vibrating absorber experiments. A value of  $M = 32$  was chosen to compute the peak amplitudes reported in the results section. A fixed value of M means that, in each

experiment, a fixed 'chunk' acquisition time has been considered for the uncertainty estimation. Because the total acquisition length varies from experiment to experiment, the 'chunk' acquisition length also varies with each experimental run.



**Figure 27 – EPFL and TUD z-scores a function of M scaling factor, rotating absorber exp. 2.**

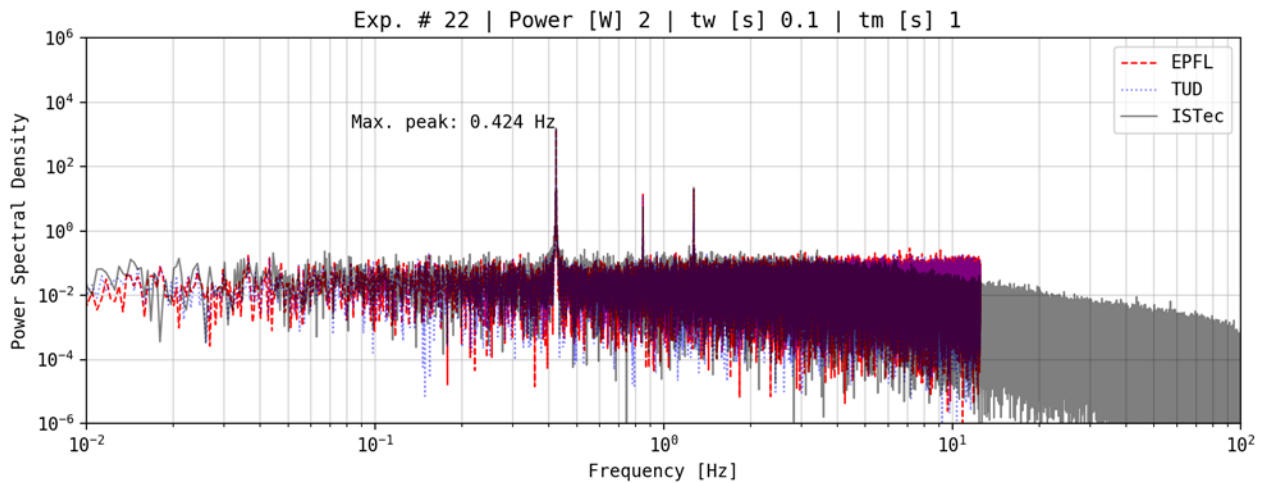


**Figure 28 – EPFL and TUD z-scores a function of M scaling factor, vibrating absorber exp. 14.**

The function that computes the uncertainty is included in Appendix 7.9 and shown in lines 38 to 51 of the `<main_daq_comparison.py>` Python wrapper.

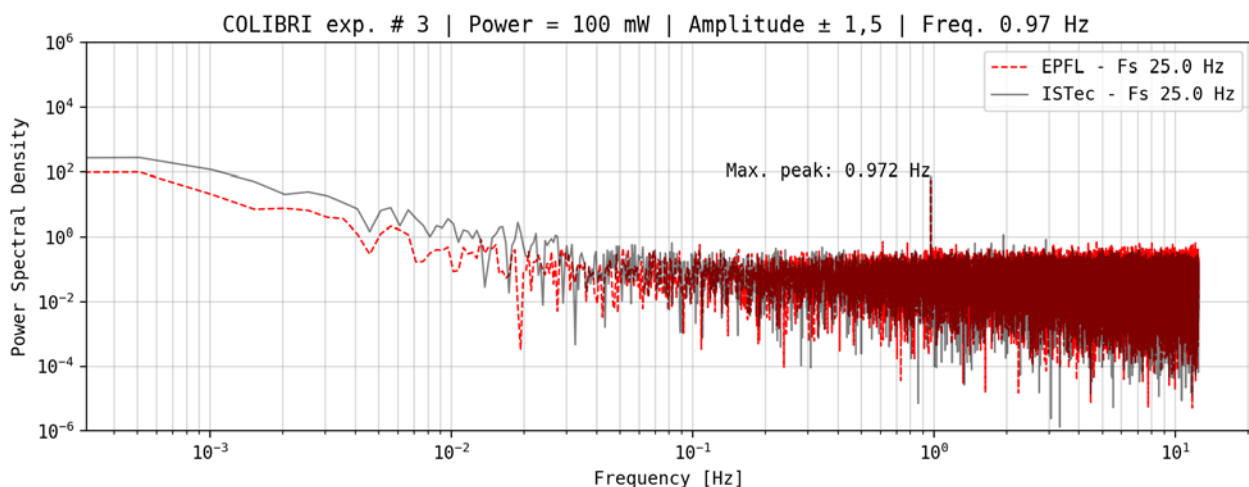
#### 4.2.3 Benchmark results

A typical power density spectrum (periodogram method) for the vibrating absorber experiment is shown in Figure 29. This example corresponds to the experiment 22 in AKR-2, where it is worth nothing that ISTec power spectrum covers a larger range of frequencies because the sampling rate is higher. However, the frequency resolution ( $\Delta f$ ) is equivalent to the other two DAQs from EPFL and TUD because the sampling frequency-to-number of data points ratio is equal for all three DAQs ( $\Delta f = \frac{f_s}{N}$ ).



**Figure 29 – Power density spectrum for vibrating absorber exp. 22 - Detector 1.**

The power density spectrum in Figure 29 shows a particular behavior for the ISTec case that is not observed for the other two acquisition systems. In the ISTec case, the PSD amplitude starts dropping at frequencies higher than a 1 Hz. This behavior suggests that ISTec DAQ contains a low pass filter with a cutoff frequency around 3 or 4 Hz and thus it was further investigated. As the ISTec SIGMA is fully optimized and graded for signals up to 100 Hz, this behavior was expected to arise from the ROBOTRON device. Thus the power density spectra from ISTec and EPFL were compared for a case where the ROBOTRON frequency-to-voltage converter was not used by ISTec SIGMA. The chosen case corresponds to a COLIBRI fuel rod oscillator measurement (exp. 3) where the DAQs input signal is coming from detector 1 that operates in current mode and hence no pulse-to-voltage conversion was required. Note that the EPFL acquisition for this detector was done with the current mode DAQ described in Section 4.1.2, and not with the pulse mode DAQ. From the power density spectra for ISTec and EPFL DAQs (Figure 30), it can be observed that ISTec PSD exhibits an amplitude decay only at frequencies higher than 100 Hz, as expected, and not at frequencies below as seen in the case where ROBOTRON is used (Figure 29). The amplitude response shown in Figure 30, for the case where ROBOTRON is not used, is consistent with the presence of the ISTec anti-aliasing low pass filter (Fix Filter Module) with a cutoff frequency of 100 Hz (see 4.1.1). A conclusion of this analysis is that ROBOTRON 20046 frequency-to-voltage converter should not be used to acquire signals with fundamental frequencies higher than 3 Hz.

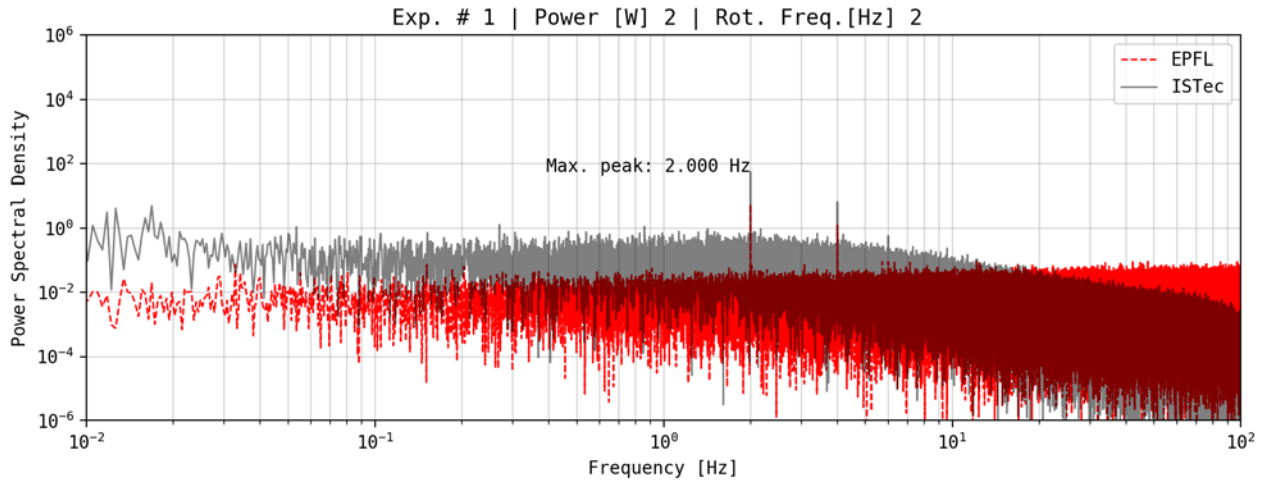


**Figure 30 – Power spectral density for COLIBRI exp. 3 - Detector 6 (current mode).**

Another important finding of this benchmark is that, for EPFL and TUD DAQs (that record counts per dwell time), a low count rate can produce larger Poisson noise fluctuations within each time step than the fluctuations due to the induced perturbation and thus lead to inaccuracies in the estimation of PSD parameters. In such a case, these inaccuracies can be reduced by downsampling the data (i.e. increasing the dwell time). This is shown in Table 7 for a rotating absorber case (experiment 1), where the EPFL peak power estimation differs by 90% if no downsampling is used, and the difference lowers to 3% if downsampling is enabled. The PSD estimates for this experiment are shown in Figure 31 for the case where EPFL data is not downsampled. The plot shows that EPFL PSD amplitude is much lower than the one from ISTec. The benchmarking results shown in this report have been therefore computed after downsampling EPFL time series to match the sampling frequency of the TUD DAQ.

**Table 7 – Downsampling effect on peak amplitude estimation – Rotating absorber exp. 1.**

	Data size	Time step [sec]	Time length [min]	Peak amp.	Rel. diff. [%]
<b>No downsampling</b>					
ISTec	594240	4.00E-03	39.6	41.9	-
EPFL	594240	4.00E-03	39.6	4.3	-89.8
<b>Downsampling by a factor of 10</b>					
ISTec	594240	4.00E-03	39.6	41.9	-
EPFL	59424	4.00E-02	39.6	40.5	-3.29



**Figure 31 – Power spectral density for rotating absorber exp. 1 – No downsampling for EPFL.**

The results of the benchmark for the rotating absorber experiments are listed in Table 8. The information contained in this table is organized as follows. The third column (*Data size*) represents the number of data points of the time series used to generate the PSD. The forth column shows the time step (inverse of sampling frequency) of the time series and the fifth column shows the total time length of the time series. The values shown on the sixth column (*M*) and onwards, have been obtained from the uncertainty quantification process described in the previous section. The sixth column indicates the divisor factor for data slicing. The seventh column (*Chunk time [min]*) represents the time length of the sliced data. The eighth column is the mean peak amplitude computed according to equation (4) and the ninth column is the relative standard deviation computed as the standard deviation, from equation (5), divided by the mean peak amplitude. The last column is z-score which has been computed according to equation (6).

It is essential to bear in mind that the reported uncertainties are dependent on the acquisition length. Therefore, the results hereby presented correspond only to a fixed '*Chunk time*' and shall not be extrapolated to other acquisition lengths.

The experiments numbers where only EPFL and ISTec results are reported, indicate that no data was measured by TUD acquisition system.



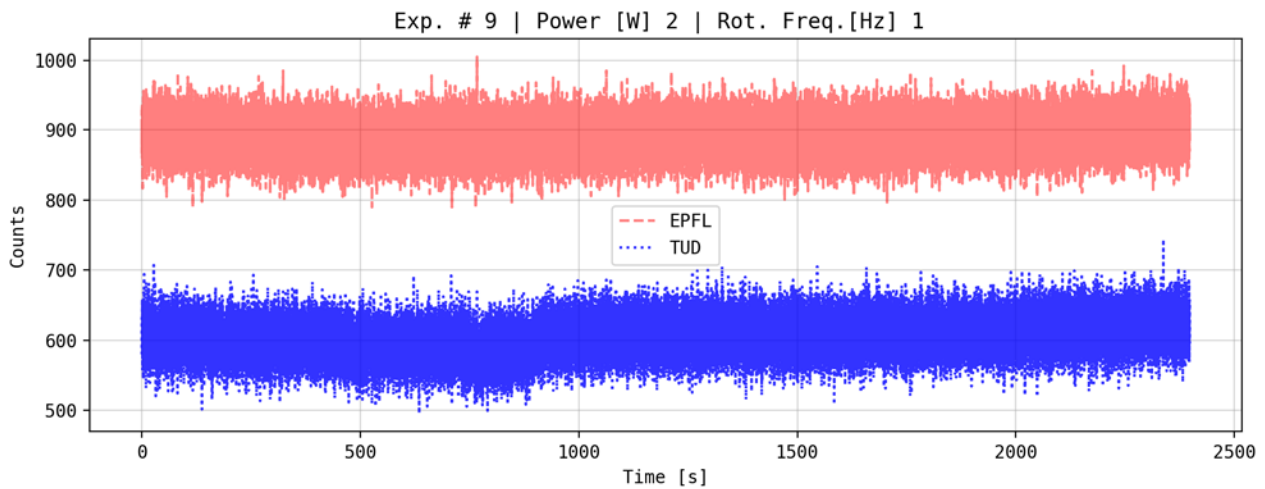
**Table 8 – Benchmarking results for rotating absorber experiments.**

#		Data size	Time step [sec]	Time length [min]	M	Chunk time [min]	Mean peak amplitude	Peak amp. std.	Rel. std. [%]	z-score
1	ISTec	594240	4.00E-03	39.6	32	1.24	1.17	0.55	46.84	-
	EPFL	59424	4.00E-02	39.6	32	1.24	0.98	0.3	30.04	-0.31
2	ISTec	596800	4.00E-03	39.8	32	1.24	1.72	0.74	42.85	-
	EPFL	59680	4.00E-02	39.8	32	1.24	1.56	0.47	30.26	-0.19
	TUD	N/A	N/A	N/A	-	-	N/A	N/A	N/A	N/A
3	ISTec	598080	4.00E-03	39.9	32	1.25	2.79	0.82	29.39	-
	EPFL	59808	4.00E-02	39.9	32	1.25	2.39	0.55	23.1	-0.4
	TUD	N/A	N/A	N/A	-	-	N/A	N/A	N/A	N/A
4	ISTec	597120	4.00E-03	39.8	32	1.24	2.58	0.68	26.51	-
	EPFL	59712	4.00E-02	39.8	32	1.24	2.17	0.57	26.41	-0.47
5	ISTec	597760	4.00E-03	39.9	32	1.25	1.49	0.57	37.99	-
	EPFL	59776	4.00E-02	39.9	32	1.25	1.62	0.51	31.36	0.17
6	ISTec	598720	4.00E-03	39.9	32	1.25	0.96	0.38	39.79	-
	EPFL	59872	4.00E-02	39.9	32	1.25	0.97	0.34	34.54	0.03
7	ISTec	597440	4.00E-03	39.8	32	1.24	1.1	0.39	35.64	-
	EPFL	59744	4.00E-02	39.8	32	1.24	1.04	0.31	30	-0.12
8	ISTec	597760	4.00E-03	39.9	32	1.25	0.86	0.22	25.29	-
	EPFL	59776	4.00E-02	39.9	32	1.25	0.92	0.36	38.59	0.14
9	ISTec	599360	4.00E-03	40	32	1.25	2.15	0.87	40.33	-
	EPFL	59936	4.00E-02	40	32	1.25	2.28	0.58	25.26	0.13
	TUD	59936	4.00E-02	40	32	1.25	1.77	0.5	28.25	-0.38
10	ISTec	599040	4.00E-03	39.9	32	1.25	0.96	0.27	28.14	-
	EPFL	59904	4.00E-02	39.9	32	1.25	0.81	0.31	38.59	-0.37

The results from Table 8 reveal that EPFL peak amplitudes estimates are comparable to those obtained with the ISTec reference system. It is worthwhile mentioning that even though the agreement is achieved because uncertainties are large in relative terms (in the order of tens of percent), the EPFL z-scores are always within 0.5 which implies that EPFL estimates less than  $0.5 \sigma_c$  away from ISTec estimates, where  $\sigma_c$  stands for the combined uncertainty (root of sum squares). Usually, an absolute value of the z-score below 2 indicates satisfactory performance, between 2 and 3, questionable performance, and above 3 unsatisfactory performance. The large uncertainties are due to low acquisition times with respect to the magnitude of the induced perturbation. As explained earlier in this section, small induced perturbation required larger acquisition times to properly resolve the fundamental frequencies of the perturbation from the rest of the contributions in the power spectrum.

TUD scores shown in Table 8 indicate that the agreement with ISTec data is satisfactory for the only reported case (exp. 9). The TUD data for experiments 2 and 3 was measured for a short time interval only and thus the analysis was not possible.

Because EPFL and TUD acquisition systems are equivalent, it is meaningful to compare their results for experiment 9. In this case, TUD system underestimates the peak value by 17%, while EPFL systems overestimates the value by 6%. These differences might be attributed to the different low-level discriminator (LLD) set ups for each acquisition system. The worst case scenario would be the one where the LLD is set too low: it results in a signal which contains gamma and electronic noise contributions along with neutron events. The different discrimination levels can be seen from the times series data shown in Figure 32. The time series plot shows that EPFL counts per dwell time is almost 50% larger than for TUD. While EPFL time series mean value is about 890 with a dispersion (standard deviation) of 24.6, the TUD time series mean value is about 603 with a dispersion of 26.5.



**Figure 32 – Time series data from TUD and EPFL systems for rot. abs. exp. 2**

The results of the benchmark for the vibrating absorber experiments are listed in Table 9. The information contained in this table is organized in the same way as for the rotating absorber experiments results explained earlier and reported in Table 8.

**Table 9 – Benchmarking results for vibrating absorber experiment.**

#		Data size	Time step [sec]	Time length [min]	M	Chunk time [min]	Mean peak amplitude	Peak amp. std.	Rel. std. [%]	z-score
11	ISTec	598080	4.00E-03	39.9	32	1.25	40.3	1.64	4.07	-
	EPFL	59808	4.00E-02	39.9	32	1.25	41.1	2.79	6.79	0.26
	TUD	59808	4.00E-02	39.9	32	1.25	40.5	1.53	3.78	0.11
12	ISTec	597760	4.00E-03	39.9	32	1.25	32.6	3.51	10.77	-
	EPFL	59776	4.00E-02	39.9	32	1.25	33.1	2.65	8.01	0.10
	TUD	59776	4.00E-02	39.9	32	1.25	32.7	2.26	6.91	0.01
13	ISTec	597760	4.00E-03	39.9	32	1.25	22.2	2.38	10.72	-
	EPFL	59776	4.00E-02	39.9	32	1.25	22.5	2.22	9.87	0.10
14	ISTec	597760	4.00E-03	39.9	32	1.25	40.8	1.65	4.04	-
	EPFL	59776	4.00E-02	39.9	32	1.25	41.3	3.12	7.55	0.13
	TUD	59776	4.00E-02	39.9	32	1.25	40.8	1.64	4.02	0
15	ISTec	297920	4.00E-03	19.9	32	0.62	22.1	2.87	12.99	-

## D2.1 Experimental report of the 1st campaign at AKR-2 and CROCUS

	<b>EPFL</b>	29792	4.00E-02	19.9	32	0.62	23.3	1.36	5.84	0.39
	<b>TUD</b>	29792	4.00E-02	19.9	32	0.62	23.8	1.14	4.79	0.55
16	<b>ISTec</b>	297920	4.00E-03	19.9	32	0.62	21.3	1.78	8.36	-
	<b>EPFL</b>	29792	4.00E-02	19.9	32	0.62	19.7	1.11	5.63	-0.74
	<b>TUD</b>	29792	4.00E-02	19.9	32	0.62	20.5	0.94	4.6	-0.41
17	<b>ISTec</b>	297920	4.00E-03	19.9	32	0.62	12.1	1.13	9.34	-
	<b>EPFL</b>	29792	4.00E-02	19.9	32	0.62	11.4	0.95	8.31	-0.47
	<b>TUD</b>	29792	4.00E-02	19.9	32	0.62	11.7	0.83	7.12	-0.29
18	<b>ISTec</b>	297920	4.00E-03	19.9	32	0.62	15.3	1.73	11.31	-
	<b>EPFL</b>	29792	4.00E-02	19.9	32	0.62	15.1	1.5	9.93	-0.08
	<b>TUD</b>	29792	4.00E-02	19.9	32	0.62	14.8	1.24	8.38	-0.22
19	<b>ISTec</b>	297600	4.00E-03	19.8	32	0.62	22.4	2.31	10.31	-
	<b>EPFL</b>	29760	4.00E-02	19.8	32	0.62	21.9	1.91	8.72	-0.16
	<b>TUD</b>	29760	4.00E-02	19.8	32	0.62	21.5	1.5	6.98	-0.30
20	<b>ISTec</b>	297920	4.00E-03	19.9	32	0.62	10.5	0.99	9.46	-
	<b>EPFL</b>	29792	4.00E-02	19.9	32	0.62	10.4	0.88	8.44	-0.03
	<b>TUD</b>	29792	4.00E-02	19.9	32	0.62	10.3	0.67	6.52	-0.11
21	<b>ISTec</b>	297920	4.00E-03	19.9	32	0.62	23.4	2.09	8.93	-
	<b>EPFL</b>	29792	4.00E-02	19.9	32	0.62	24.3	1.93	7.94	0.32
	<b>TUD</b>	29792	4.00E-02	19.9	32	0.62	24.1	1.07	4.44	0.26
22	<b>ISTec</b>	597760	4.00E-03	39.9	32	1.25	35.4	2.12	5.99	-
	<b>EPFL</b>	59776	4.00E-02	39.9	32	1.25	33.2	1.79	5.39	-0.80
	<b>TUD</b>	59776	4.00E-02	39.9	32	1.25	33.9	1.8	5.31	-0.52
23	<b>ISTec</b>	297280	4.00E-03	19.8	32	0.62	23.2	1.41	6.08	-
	<b>EPFL</b>	29728	4.00E-02	19.8	32	0.62	23	1.55	6.74	-0.11
	<b>TUD</b>	29728	4.00E-02	19.8	32	0.62	23.7	1.21	5.11	0.26
24	<b>ISTec</b>	299200	4.00E-03	19.9	32	0.62	14.7	1.49	10.14	-
	<b>EPFL</b>	29920	4.00E-02	19.9	32	0.62	13.4	1.62	12.09	-0.59
	<b>TUD</b>	29920	4.00E-02	19.9	32	0.62	13.9	1.38	9.93	-0.37
25	<b>ISTec</b>	599040	4.00E-03	39.9	32	1.25	46.2	3.24	7.01	-
	<b>EPFL</b>	59904	4.00E-02	39.9	32	1.25	43.2	2.81	6.5	-0.69
	<b>TUD</b>	59904	4.00E-02	39.9	32	1.25	44.4	3.14	7.07	-0.40
26	<b>ISTec</b>	299200	4.00E-03	19.9	32	0.62	11.4	0.99	8.66	-
	<b>EPFL</b>	29920	4.00E-02	19.9	32	0.62	10.6	0.81	7.65	-0.61
	<b>TUD</b>	29920	4.00E-02	19.9	32	0.62	10.9	0.78	7.18	-0.39
27	<b>ISTec</b>	299200	4.00E-03	19.9	32	0.62	11.8	1.03	8.73	-
	<b>EPFL</b>	29920	4.00E-02	19.9	32	0.62	10.9	0.93	8.55	-0.63

Before discussing the performance of the acquisition systems for the vibrating absorber experiments, it is meaningful to observe in Table 9 that the relative uncertainties displayed in the second-to-last column (*Rel. std. [%]*) are approximately one order of magnitude lower than for the rotating absorber experiments cases reported in Table 8. The fact that the uncertainties associated to the rotating absorber experiments are larger than those from the vibrating absorber ones can be explained by

the weaker signal-to-unwanted-noise<sup>1</sup> ratios for the former and hence longer acquisition times would be needed to achieve the same level of uncertainties.

Concerning the DAQs performance, the results listed in Table 9 suggest that EPFL peak amplitudes estimates are, once again, comparable to those obtained with the ISTec reference system. EPFL system z-scores are always below 0.8, which is noteworthy considering that the uncertainties are substantially lower than for the rotating absorber experiments.

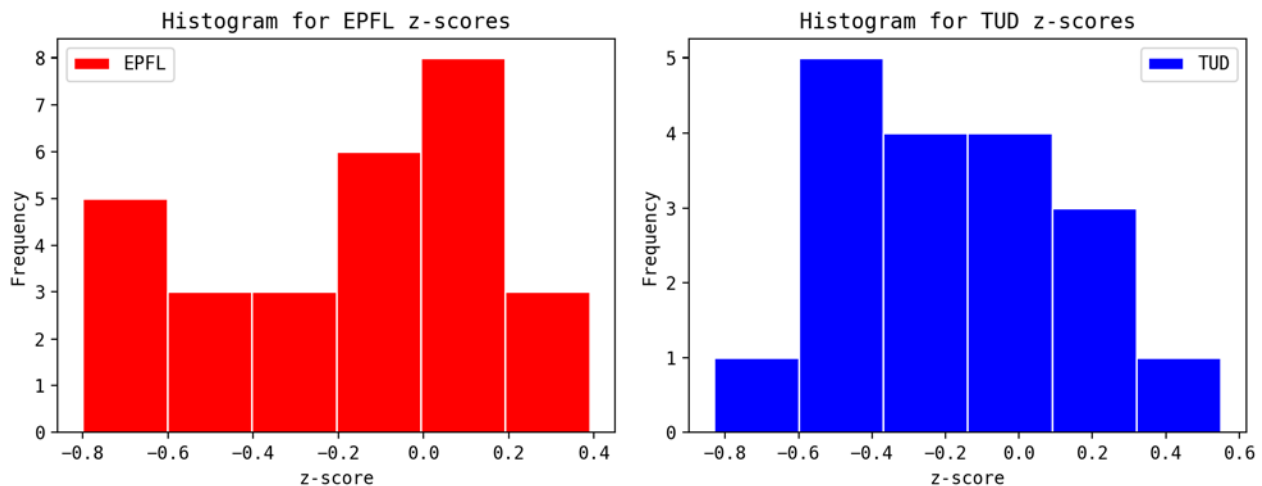
The z-scores for TUD acquisition system are, as in the EPFL cases, always below 0.8 and therefore the peak amplitude estimates are equally comparable to those obtained with the ISTec reference.

Finally, the benchmark results for the vibrating fuel rods experiments are listed in Table 10. The comparison between the three DAQs was only possible for the exp. 3, using the signal from detector 8 (in-core BF<sub>3</sub> located next to the COLIBRI fuel vibrating device).

**Table 10 - Benchmarking results for the CROCUS vibrating fuel rods experiments**

#		Data size	Time step [sec]	Time length [min]	No. of chunks (M)	Chunk size	Chunk length [min]	Mean peak amplitude	Peak amp. std.	Rel std [%]	z-score
3	ISTec	449248	4E-03	29.9	32	14039	0.9	0.42	0.26	61.90	-
	EPFL	59904	3E-02	30.0	32	1872	0.9	0.44	0.08	18.18	0.08
	TUD	59904	3E-02	30.0	32	1872	0.9	0.43	0.07	16.28	0.04

The results from Table 10 show that the relative uncertainties for the peak amplitude estimates are large (in the order of tens of percent), whereas the z-scores are limited to small values. This suggests that a good agreement was achieved between ISTec, TUD and EPFL peak amplitude estimates. Recall that the combination of large uncertainties and small z-score values was already observed for the rotating absorber experiments. In the case of the vibrating fuel rods experiments, the large uncertainties reported in Table 10 are also resulting from the low acquisition times with respect to the magnitude of the induced perturbation.



**Figure 33 – Frequency distribution of EPFL and TUD z-scores for all experiments**

The results for the rotating absorber, vibrating absorber and COLIBRI experiments are shown altogether in the form of a z-scores frequency distribution for a global overview in Figure 33. It shows

<sup>1</sup> Here 'signal' refers to the fluctuations due to the induced perturbations and 'unwanted noise' refers to the neutron chain random fluctuations and other detection noise (see Section 4.2.2).

the EPFL and TUD z-score histograms for all experimental cases. It is possible to observe in the figure that the z-scores from EPFL and TUD acquisition systems are bounded practically by the same interval.

Concerning the signs, the EPFL z-scores are negative for 17 out of 28 cases (61%), and for TUD the sign is negative for 11 out of 18 cases (61%). The mean z-score value is -0.18 for EPFL and -0.17 for TUD, which may suggest a minor underestimation trend for both systems.

Even though the results presented in this benchmark are dependent on the acquisition time (chunk times), they represent an upper bound of the differences we can find for longer acquisition times. Accordingly, longer acquisition times would allow to better resolve differences because the uncertainty levels would be lower. Overall, it is safe to conclude that, for the given acquisition times, both EPFL and TUD acquisition systems can accurately reproduce the results obtained by the ISTec reference system.

## 5 Conclusion

In the framework of the CORTEX project, the work package 2 targets the generation of high quality neutron noise experimental data for the subsequent validation of computers methods and models developed in work package 1.

In this aim, the first campaigns in the TUD AKR-2 and EPFL CROCUS zero power experimental reactors were successfully carried out in March and September 2018. It consisted in measurements in reference static states, and with mechanical perturbations arising from rotating and vibrating absorbers, and from vibrating fuel rods, respectively. The present report documents the experimental setups and measurements for each facility and perturbation type.

In addition, acquisition systems from all three contributing partners were first described, and then benchmarked using the data mainly from the AKR-2 campaign. The main purpose of the benchmark was to qualify TUD and EPFL acquisition systems against the ISTec Sigma system (subtask 2.1.1), which was set as the reference DAQ as it was qualified and tested in industrial environments. The benchmark, which focuses on the comparison of peak amplitudes obtained from the frequency domain analysis, revealed that, for all the experimental cases and the given acquisition times, EPFL and TUD data acquisition systems are capable of reproducing results obtained by the ISTec system. The benchmark allowed also to conclude that, EPFL and TUD systems exhibit an analogous behaviour as the z-scores are bounded practically by the same values and their mean values are identical.

Following this report, the noise experimental data will be prepared and distributed to the members of the consortium in the form of raw time series, and a few examples of power spectral densities.



## 6 References

- [1] B. Boehmer, M. Grantz, W. Hansen, D. Hinke, J. Konheiser, H.-C. Mehner, K. Noack, R. Schneider, I. Stephan, and S. Unholzer, "Investigation of Gamma and Neutron Energy Fluences in Iron -Water Benchmark Configurations for the Verification of Monte Carlo Calculations and their Application in Reactor Material Dosimetry," *J. Nucl. Sci. Technol.*, vol. 39, no. sup2, pp. 947–950, 2002.
- [2] U. Kasemeyer, R. Früh, J. M. Paratte, and R. Chawla, "Benchmark on Kinetic Parameters in the CROCUS Reactor," in *International Reactor Physics Experiments Handbook (IRPhE)*, no. 4440, OECD, Ed. 2007, p. 94.

## 7 Appendices

### 7.1 AKR-2 reactor data summary

<i>Reactor Vessel:</i>	Total Diameter:	250 cm
	Total Height:	350 cm (reactor vessel 280 cm)
<i>Fuel Elements:</i>	Plates:	250 mm diameter, height 2-23 mm
	Material:	Homogeneous mixture from Uranium oxide (UO <sub>2</sub> , enrichment 19.8 %) and PE
	Critical Mass:	794 g of <sup>235</sup> U
<i>Reflector:</i>	Material:	Pure graphite ( $\rho = 1.75 \text{ g/cm}^3$ )
	Thickness:	32 cm radial, 20 cm axial
<i>Neutron Source:</i>	Am-Be:	Source strength: $2.2 \cdot 10^6 \text{ n/s}$
<i>Control Rods:</i>	3 independent combined control and safety rods	
	Material:	Cadmium (0.5 mm thick sheets)
	Total reactivity:	About 37 ¢ per rod
<i>Nuclear Instrumentation:</i>	2 logarithmic wide-range channels with fission chamber detectors	
	1 linear power-range channel with $\gamma$ -compensated ion chamber	
<i>Biological Shield:</i>	axial:	48 cm heavy concrete
	radial:	15 cm paraffin and 58 cm heavy concrete
<i>Experimental Irradiation Channels:</i>	horizontal:	4, $\phi_{\text{max}} = 2.5 \cdot 10^7 \text{ n/(cm}^2 \cdot \text{s)}$
	vertical:	2
<i>Fast Shut-Down Possibilities:</i>	drop down of the lower core section for about 5 cm	
	drop down of the 3 control rods	
<i>Maximum Excess Reactivity:</i>	0.3 %	
<i>Maximum Continuous Power:</i>	2 W	

## 7.2 AKR-2 reactor kinetic data

The following data has been computed using the SERPENT 2.1.16 and MCNP 6.0 codes with the ENDF/B-VII.1 and ENDF/B-VIII.0 nuclear data libraries, respectively.

**Table 11 – AKR-2 reactor kinetic data.**

		Serpent 2 ENDF/B-VII.1		MCNP 6.0 ENDF/B-VIII.0	
		Estimate	Standard deviation	Estimate	Standard deviation
Generation time	$\Lambda$	$5.78 \times 10^{-5} \text{ s}$	$3.18 \times 10^{-8} \text{ s}$	$5.73 \times 10^{-5} \text{ s}$	$8.50 \times 10^{-8} \text{ s}$
Beta effective	$\beta_{\text{eff}}$	769 pcm	2 pcm	766 pcm	4 pcm
Rossi-Alpha	$\alpha$	$-133 \text{ s}^{-1}$	$2.60 \times 10^{-1} \text{ s}^{-1}$	$-134 \text{ s}^{-1}$	$7.90 \times 10^{-1} \text{ s}^{-1}$

**Table 12 - AKR-2 reactor kinetic data – 6-group delayed neutron data.**

	Precursor	$\beta_{\text{eff}}$	Std. dev.	$\lambda_i \text{ (s}^{-1}\text{)}$	Std. dev.
<b>Serpent 2</b>	1	0.000268	0.000003	0.01334	< 0.00001
	2	0.001385	0.000006	0.03273	< 0.00001
	3	0.001349	0.000006	0.12079	< 0.00001
	4	0.002951	0.000009	0.30293	< 0.00001
	5	0.001234	0.000006	0.85008	< 0.00001
	6	0.000508	0.000004	2.85513	< 0.00001
<b>MCNP 6.0</b>	1	0.00027	0.00001	0.01334	< 0.00001
	2	0.00137	0.00002	0.03273	< 0.00001
	3	0.00133	0.00002	0.12079	< 0.00001
	4	0.00296	0.00003	0.30293	< 0.00001
	5	0.00123	0.00002	0.85011	0.00001
	6	0.00050	0.00001	2.85508	0.00003

### 7.3 AKR-2 detectors position

7.3.1 Detectors 1 and 2 positions (channel 5-6) for the AKR-2 first campaign, 120 cm above the ground.

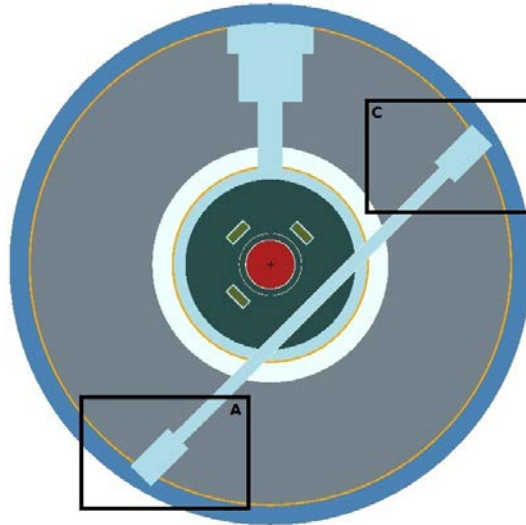


Figure 34 – Section of the Lower Tangential Channel (5-6) of the AKR-2.

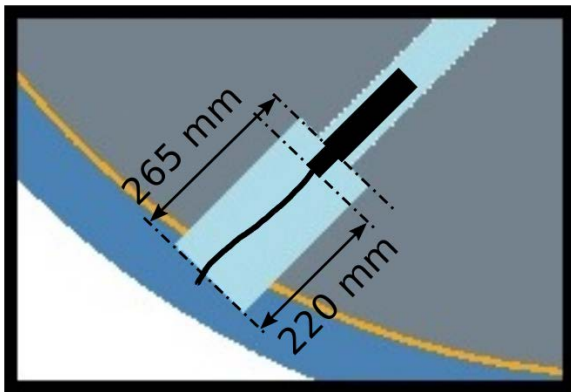


Figure 35 – Position of Detector 1.

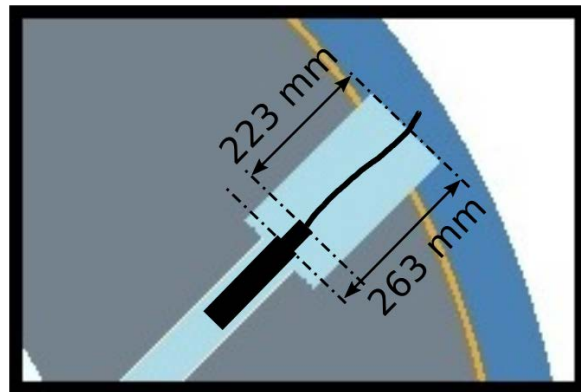


Figure 36 – Position of Detector 2.

7.3.2 Detector 3 position (channel 1-2) for the AKR-2 first campaign, 130 cm above the ground.

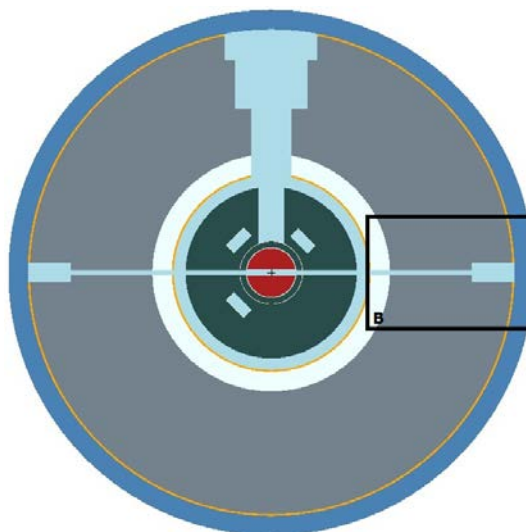
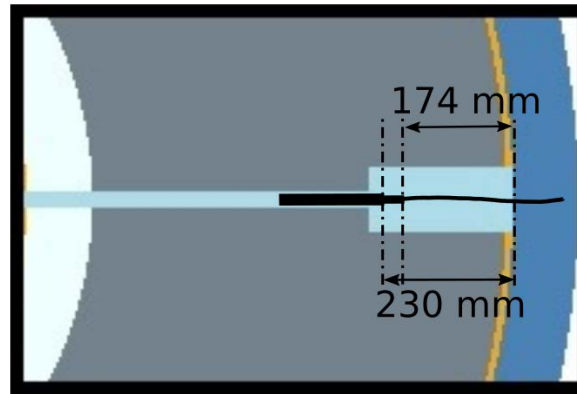


Figure 37 – Section of the Central Channel (1-2) of the AKR-2.



**Figure 38 – Position of Detector 3.**

## 7.4 Neutron measurement channels for the AKR-2 campaign

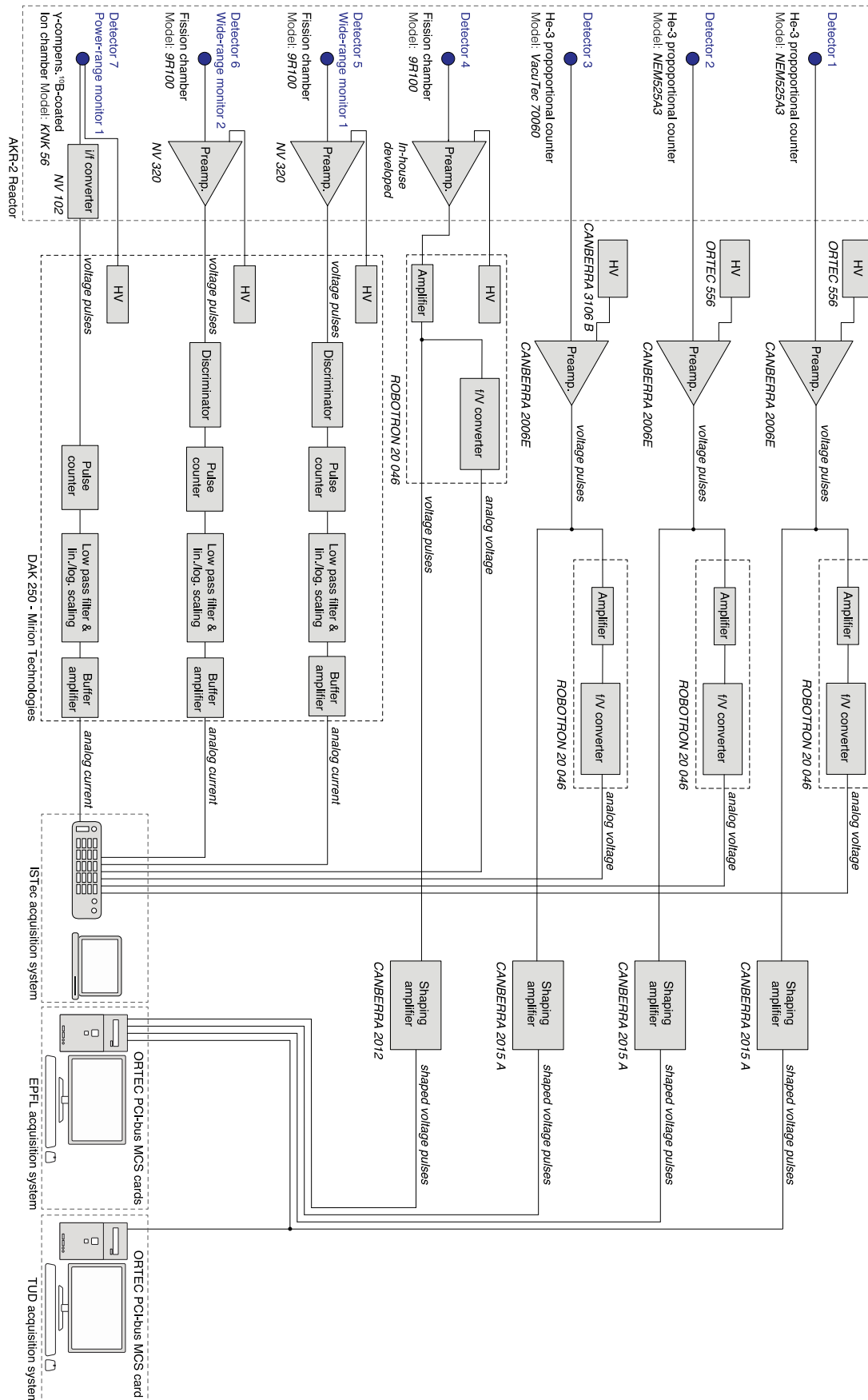



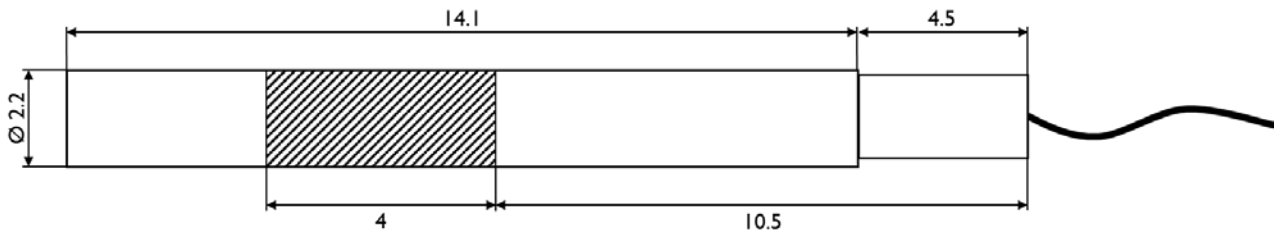
Figure 39 – Neutron measurement channels for the AKR-2 campaign.



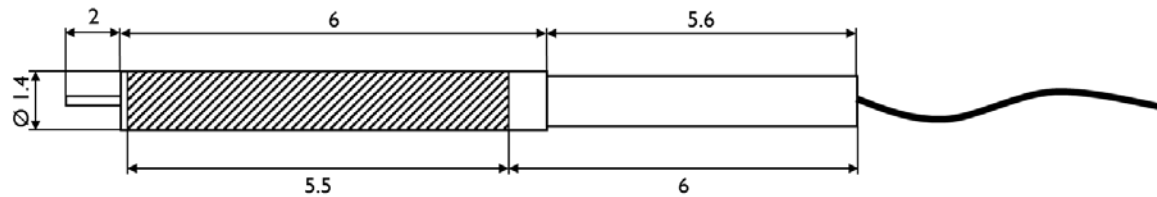
## 7.5 Specifications of the detectors of the AKR-2 campaign

### 7.5.1 $^3\text{He}$ proportional counters

Detector 1 and 2  Estimated active zone,  $V = 15.205 \text{ cm}^3 (+ 1.83 \text{ cm}^3 / - 1.70 \text{ cm}^3)$



Detector 3  Estimated active zone,  $V = 8.467 \text{ cm}^3 (+ 1.43 \text{ cm}^3 / - 1.83 \text{ cm}^3)$



**Figure 40 – Schematic of the  $^3\text{He}$  proportional counters, i.e. detectors 1 to 3, used in the channels 5, 6 and 2, respectively.**

### 7.5.2 $^{235}\text{U}$ fission chamber and reactor monitors

Information on these detectors were extracted from AKR-2 safety report (detectors 5 and 6), and from pictures taken during it refurbishment (detectors 4 and 7).

**Table 13 – Dimensions of AKR-2 fission chambers and compensated ionization chambers.**

#	Name	Type	Sensitive material	Shape	Length (cm)	Diameter (cm)	Source
4	-	FC	$^{235}\text{U}$ coating	Cylindrical	$33.0 \pm 1.0$	$4.8 \pm 1.0$	Photo
5	WRM1	FC	$^{235}\text{U}$ coating	Cylindrical	$11.2 \pm 0.1$	$3.1 \pm 0.1$	Safety report
6	WRM2	FC	$^{235}\text{U}$ coating	Cylindrical	$11.2 \pm 0.1$	$3.1 \pm 0.1$	Safety report
7	PRM1	CIC	$^{10}\text{B}$ coating	Cylindrical	$12.9 \pm 2.0$	$4.7 \pm 1.0$	Photo

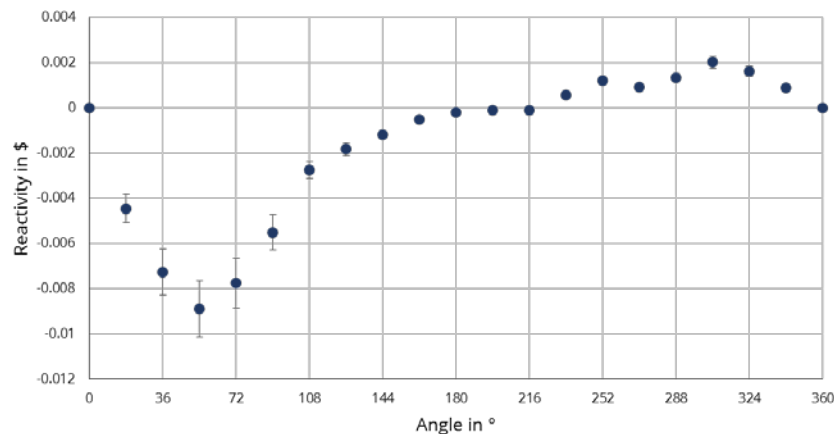
## 7.6 Reactivity worth of AKR-2 perturbation systems

### 7.6.1 Rotating absorber

The total reactivity of the absorber is 1.09 cent, with an amplitude of 0.545 cents and a mean of -0.34 cents ( $\beta_{\text{eff}}=766$  pcm).

**Table 14 – Measured reactivity of the rotating absorber.**

Angle (°)	0	18	36	54	72	90	108	126	144	162
Reactivity (\$)	0	-0.00446	-0.00728	-0.00888	-0.00776	-0.00551	-0.00274	-0.00184	-0.00119	-0.00051
Angle (°)	180	198	216	234	252	270	288	306	324	342
Reactivity (\$)	-0.00020	-0.00010	-0.00010	0.00055	0.00121	0.00092	0.00133	0.00202	0.00162	0.00087



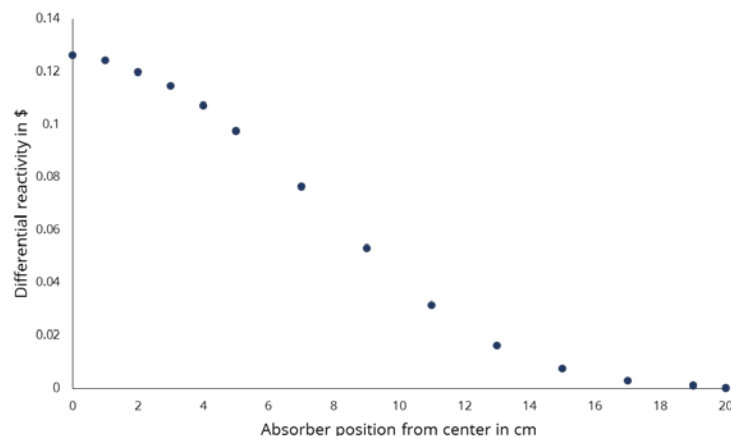
**Figure 41 – Measured reactivity of the rotating absorber.**

### 7.6.2 Linear moving absorber

The total reactivity of the absorber is 1.26 cent ( $\beta_{\text{eff}}=766$  pcm).

**Table 15 – Measured reactivity of the linear moving absorber.**

Position (cm)	0	1	2	3	4	5	7
Reactivity (\$)	0.126247	0.124423	0.119949	0.114524	0.107112	0.097519	0.076369
Position (cm)	9	11	13	15	17	19	20
Reactivity (\$)	0.053138	0.031531	0.016183	0.007546	0.002772	0.001108	0



**Figure 42 – Measured reactivity of the linear moving absorber.**

## 7.7 Neutron measurement channels for the CROCUS campaign

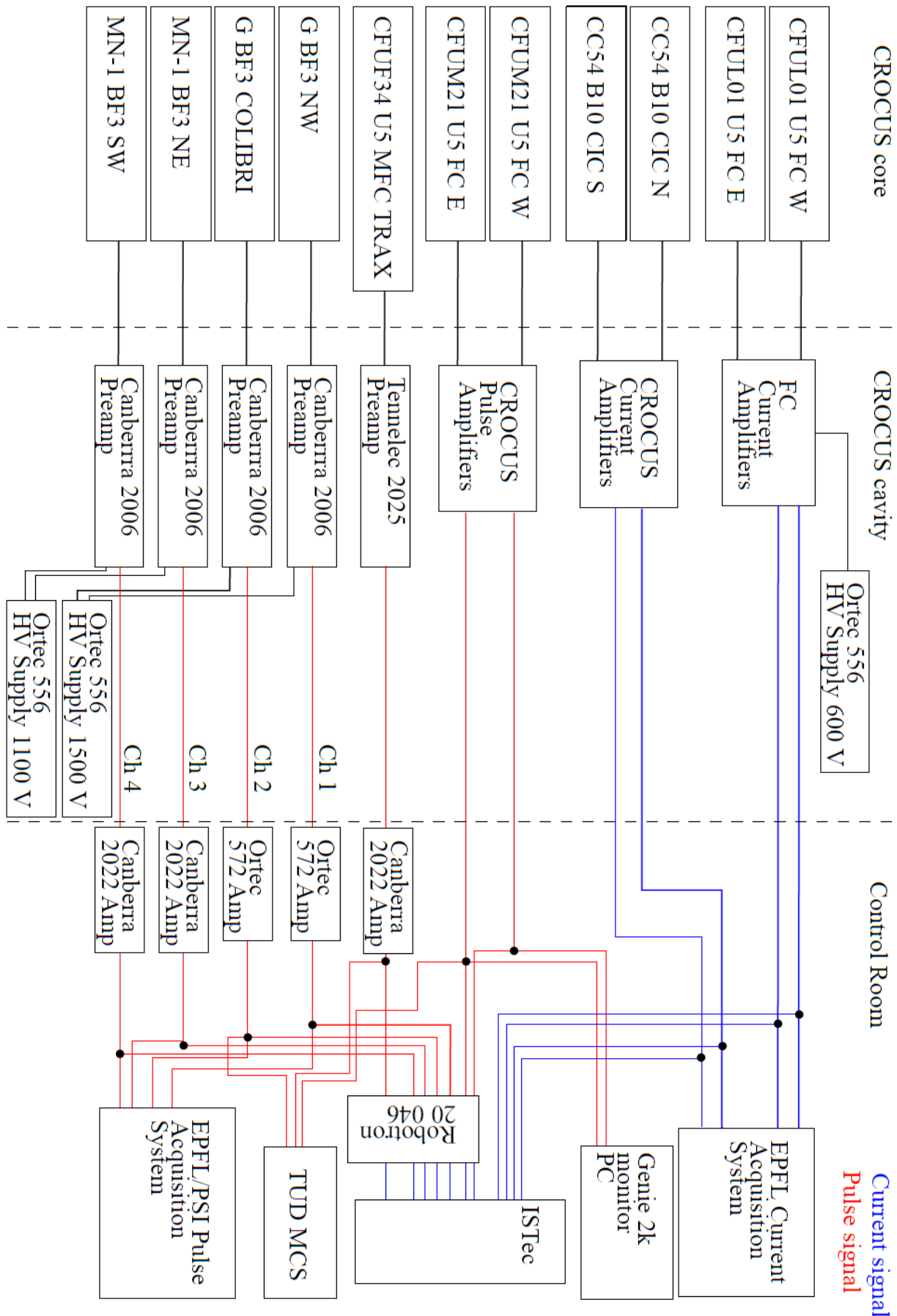


Figure 43 – Neutron measurement channels for the CROCUS campaign.

## 7.8 Specifications of the detectors of the CROCUS campaign

### 7.8.1 Photonis CFUL01 fission chamber

The Photonis CFUL01 fission chamber consists in a large tube with a 1-g  $^{235}\text{U}$  coating, the internals are described in Figure 44. During the experimental campaign, it was set first in a Faraday cage consisting in an aluminum tubing, and then inserted in a PMMA in-air experimental channel, all set vertically below the superior grid (see Figure 45).

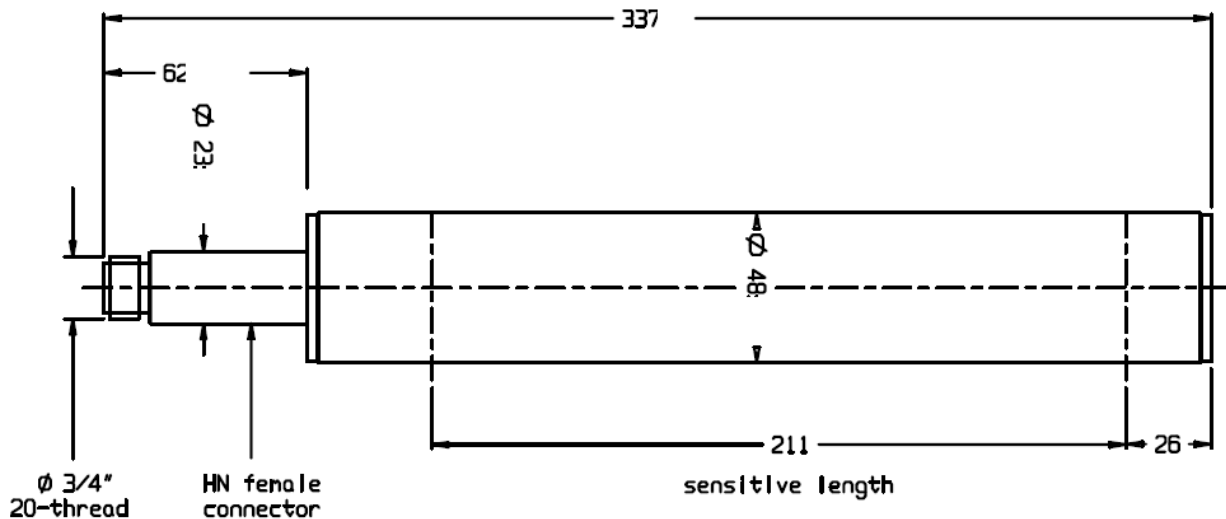


Figure 44 – Schematic of the Photonis CFUL01 fission chamber.

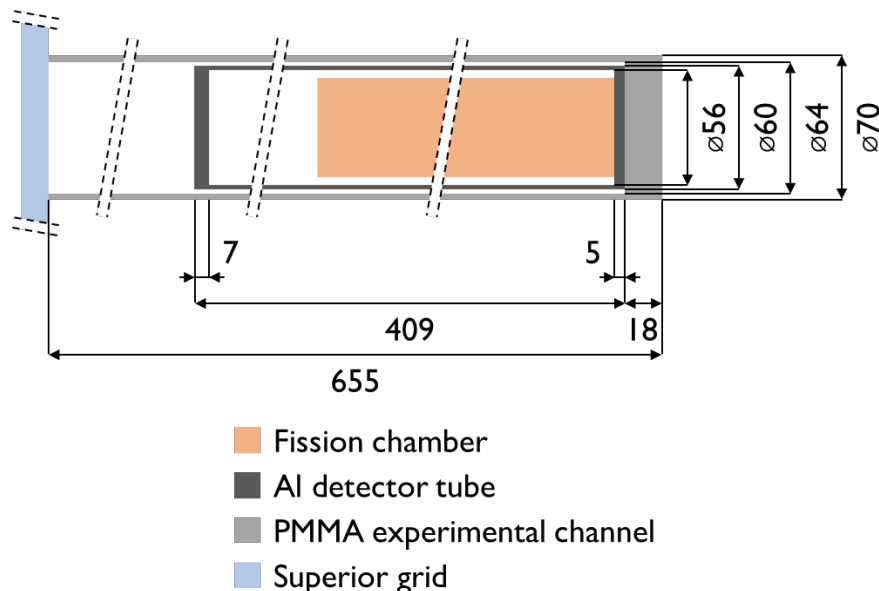


Figure 45 – Schematic of the fission chamber tube and in-air experimental channel with respect to the superior grid. NB: the channel is set vertically in-core, left side is top.

### 7.8.2 $\text{BF}_3$ proportional counters

Two types of  $\text{BF}_3$  proportional counters were employed. Limited specification is available from the manufacturers for the Transcommerce International MN-1 detectors, and an x-ray image of the internals was carried out confirming them (see Figure 46). For the other and smaller  $\text{BF}_3$  “grey” detectors, no information is available, neither series nor manufacturer. An x-ray image is considered, for now only the external dimensions are available. A summary of available information is presented in Table 16. One MN-1 PC was set in a control rod guide tube (equivalent to a  $\text{U}_{\text{metal}}$  cladding), the others were installed in in-air experimental channels lying at the bottom of the core, and whose diameter dimensions are presented in Figure 47.

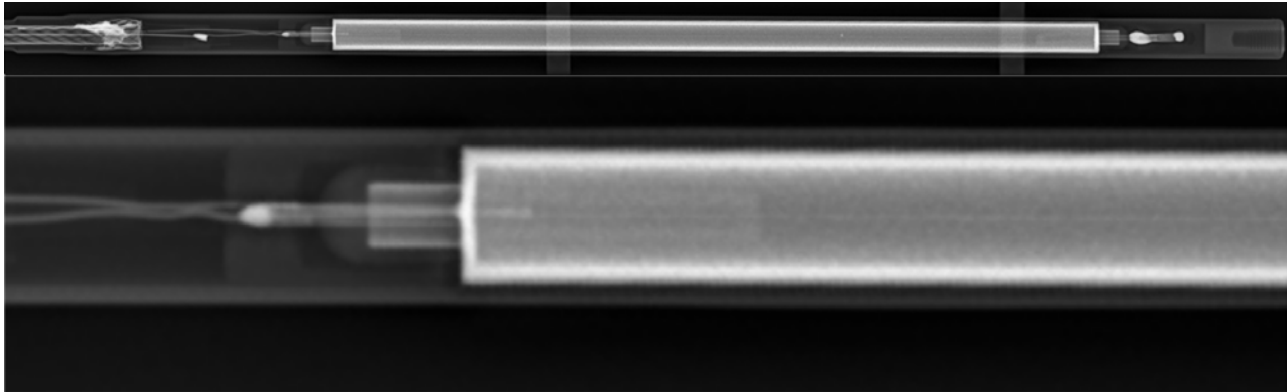


Figure 46 – X-ray image of a Transcommerce International MN-1 detector.

Table 16 – Specifications of the  $\text{BF}_3$  proportional counters, from the supplier in the case of the Transcommerce International MN-1 detector, measured (casing) and estimated (active) for the “grey” smaller detector.

Supplier	Detector	Length (cm)			Diameter (cm)	
		Total	Al casing	Active	Al casing	Active
Trans. International	MN-1	25	18.4	12.7	7.5	6.3
Unknown	“Grey”	-	14.1	est. ~8.4	7.5	est.~6.3

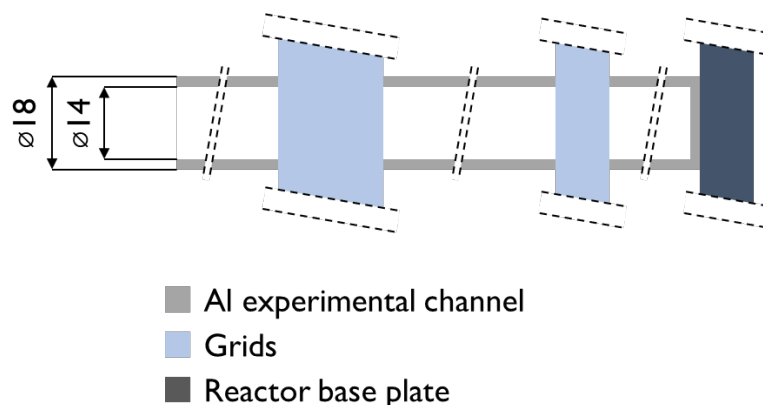
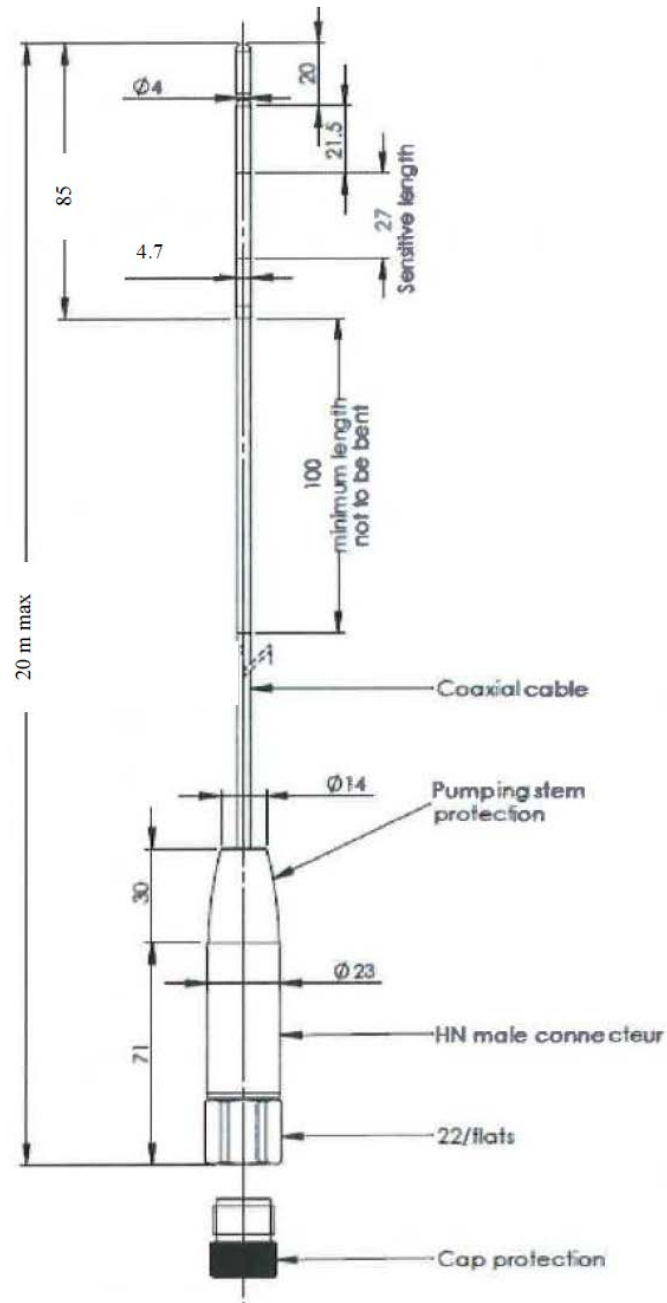


Figure 47 – Schematic of the in-air aluminum experimental channel used by one MN-1 and both “grey”  $\text{BF}_3$  proportional counters, with respect to the grids and the reactor base plate. NB: the channel is set vertically in-core, left side is top.

### 7.8.3 Photonis CFUF34 miniature fission chamber (TRAX)

The Photonis CFUF34 1-mg  $^{235}\text{U}$ -coated miniature fission chamber is part of the CROCUS reactor system called TRAX. It allows translating radially and axially this watertight miniature detector along the slit between the two superior half-grids. It was set at core center during the whole measurement campaign.



**Figure 48 – Schematic of the Photonis CFUF34 miniature fission chamber. NB: the detector's side is at the bottom when set in-core.**



## 7.9 Scripts for data acquisition benchmark

< main\_daq\_comparison.py >

```

1. import numpy as np; import os; import pandas as pd; import sys
2. import matplotlib.pyplot as plt; import matplotlib as mpl;
3. from scipy.ndimage.interpolation import shift; import math
4. from IPython import get_ipython
5. from scipy import signal
6.
7. caseselection = 1 # Select experiment number
8. cases = pd.read_csv('~/akr2_experiment_cases.csv', sep=';')
9. idx = caseselection - 1
10.
11. istec_filename = cases.values[idx, 1]
12. epfl_filename = cases.values[idx, 2]
13. tud_filename = cases.values[idx, 3]
14. casename = cases.values[idx, 4]
15. istec_dclevel = cases.values[idx, 5]
16. istec_trigger_pos = cases.values[idx, 6]
17. epfl_trigger_pos = cases.values[idx, 7]
18.
19. # %% Flags
20. ds_flag = 1 # Downsampling data
21. m = 32 # number of samples for uq
22.
23. # %% Functions
24. def standarize(data):
25.     """Standarize datasets by removing the mean and normalizing by std"""
26.     data -= data.mean()
27.     data /= data.std()
28.     return data
29.
30. def psd(data, dwell):
31.     """Returns the power spectral density using the periodogram method"""
32.     N = len(data)
33.     freq = np.fft.fftfreq(N, dwell); freq=freq[:int(N/2)]
34.     Y = np.fft.fft(data); Y=Y[:int(N/2)]
35.     psd = abs(np.square(Y)) * 2 * dwell / N
36.     return freq, psd
37.
38. def maxfreq(freq, psd, min_freq):
39.     """Returns the maximum peak bin position, frequency and amplitude"""
40.     cutoff = max(np.where(freq <= min_freq)[0])
41.     N = len(freq)
42.     peakamp = max(psd[cutoff:N])
43.     maxpos = np.where(psd == peakamp)[0]
44.     maxfreq = freq[maxpos]
45.     if len(maxfreq) > 1:
46.         maxfreq = maxfreq[0]
47.     return maxpos, maxfreq, peakamp
48.
49. def downsample(data, factor):
50.     """Downsamples the data by a factor of 'factor'"""
51.     ds_data = data.reshape(-1, factor).mean(axis=1)
52.     return ds_data
53.
54. def psd_uq(data, dwell, M):
55.     """Returns the peak amplitude uncertainty"""
56.     N = len(data)
57.     data_rs = data.reshape(-1, int(N/M)) # reshape into M rows of N/M elements each
58.     peakamp_rs = []
59.     for i in range(0, M):
60.         f, p = psd(data_rs[i, :], dwell)
61.         _, _, peakamp = maxfreq(f, p, 0.1)
62.         peakamp_rs.append(peakamp)
63.     peakamp_rs = np.asarray(peakamp_rs)

```

```

64.     sigma_amp = np.std(peakamp_rs)
65.     mean_amp = np.mean(peakamp_rs)
66.     return mean_amp, sigma_amp
67.
68. # %% Reading EPFL data #####
69. epfl_filepath = os.path.join('/2.1.2_data/epfl/', epfl_filename)
70. epfl_triggerpath = epfl_filepath.replace('card1', 'card4')
71. get_ipython().run_line_magic('run', '-i ./modules/epfl_module')
72.
73. # %% Reading ISTec data #####
74. istec_filepath = os.path.join('/2.1.2_data/istec/', istec_filename)
75. get_ipython().run_line_magic('run', '-i ./modules/istec_module')
76.
77. # %% Reading TUD data #####
78. if isinstance(tud_filename, str) == True:
79.     tud_filepath = os.path.join('/2.1.2_data/tud/', tud_filename)
80.     get_ipython().run_line_magic('run', '-i ./modules/tud_module')
81.
82. ## Results
83. zscore_epfl = (epfl_mean_amp -
84.                 istec_mean_amp) / np.sqrt(epfl_sigma_amp**2 + istec_sigma_amp**2)
85. if isinstance(tud_filename, str) == True:
86.     zscore_tud = (tud_mean_amp -
87.                   istec_mean_amp) / np.sqrt(tud_sigma_amp**2 + istec_sigma_amp**2)

```

< epfl\_module.py >

```

1. #####
2. # Reading EPFL data #####
3. #####
4. # load main data file
5. epfl_data = np.loadtxt(epfl_filepath)
6.
7. # determine no. of sweeps and dwell time based on no. of sweeps
8. # dwell = 40 ms if sweeps=1, 4 ms if sweeps = 10
9. if len(epfl_data.shape) > 1:
10.     sweeps = epfl_data.shape[1]
11.     epfl_dwell = 0.004
12.     epfl_data_new = np.zeros(epfl_data.shape)
13.     for j in range(0, sweeps):
14.         epfl_data_new[:,j] = (shift(epfl_data[:,j], 215*(j), cval=np.mean(epfl_data))) # s
15.         hift 215 bins and replace by zeros the first bins
16.     epfl_data = np.ndarray.flatten(epfl_data_new, order='F')
17. else:
18.     sweeps = 1
19.     epfl_dwell = 0.04
20.
21. # Cutting data for time sync
22. epfl_data = epfl_data[epfl_trigger_pos:]
23.
24. if ds_flag == 1 and epfl_dwell < 0.04:
25.     N_epfl = int(len(epfl_data)/10)*10
26.     epfl_data = epfl_data[0:N_epfl]
27.
28.     epfl_data = downsample(epfl_data, 10)
29.     epfl_dwell *= 10
30.
31.     N_epfl = int(len(epfl_data)/m)*m # Make it divisible by m
32.     epfl_data = epfl_data[0:N_epfl]
33.     epfl_time = np.arange(0, N_epfl, 1)*epfl_dwell
34. else:
35.     N_epfl = int(len(epfl_data)/m)*m # Make it divisible by m
36.     epfl_data = epfl_data[0:N_epfl]
37.     epfl_time = np.arange(0, N_epfl, 1)*epfl_dwell
38.
39. epfl_data = standarize(epfl_data)

```

```

40. epfl_freq, epfl_psd = psd(epfl_data, epfl_dwell)
41.
42. epfl_maxpos, epfl_maxfreq, epfl_peakamp = maxfreq(epfl_freq, epfl_psd, 0.1)
43.
44. epfl_mean_amp, epfl_sigma_amp = psd_uq(epfl_data, epfl_dwell, m)

```

< istec\_module.py >

```

1. #####
2. # Reading ISTec data #####
3. #####
4. # load main data file in chunks
5.
6. istec_rawdata = pd.read_csv(istec_filepath, chunksize=100000)
7. istec_time = list()
8. istec_data = list()
9. istec_trigger = list()
10. for chunk in istec_rawdata:
11.     istec_time.append(chunk.values[:,2]) # Time vector
12.     istec_data.append(chunk.values[:,3]) # Detector 1
13. istec_time = np.hstack(istec_time)
14. istec_data = np.hstack(istec_data)
15.
16. istec_time = istec_time[istec_trigger_pos:-1]-
    istec_time[istec_trigger_pos] # correct the time vector in size and shift
17. istec_data = istec_data[istec_trigger_pos:-1]
18.
19. # Cutting end of data to match time lenght with EPFL
20. istec_dwell = 0.004
21. istec_final_bin = int(N_epfl*epfl_dwell/istec_dwell)
22.
23. istec_time = istec_time[0:istec_final_bin]
24. istec_data = istec_data[0:istec_final_bin]
25.
26. istec_data = standarize(istec_data)
27.
28. istec_freq, istec_psd = psd(istec_data, istec_dwell)
29.
30. istec_maxpos, istec_maxfreq, istec_peakamp = maxfreq(istec_freq, istec_psd, 0.1)
31.
32. istec_mean_amp, istec_sigma_amp = psd_uq(istec_data, istec_dwell, m)

```

< tud\_module.py >

```

1. #####
2. # Reading TUD data #####
3. #####
4. # load main data file
5. tud_rawdata = pd.read_csv(tud_filepath, sep=' ')
6. tud_time = tud_rawdata.values[:,0]
7. tud_data = tud_rawdata.values[:,1]
8.
9. tud_dwell = tud_time[4] - tud_time[3]
10.
11. # Cutting end of data to match time lenght with EPFL
12. tud_final_bin = int(round(N_epfl*epfl_dwell/tud_dwell))
13. tud_time = tud_time[0:tud_final_bin]
14. tud_data = tud_data[0:tud_final_bin]
15.
16. tud_data = standarize(tud_data)
17.
18. tud_freq, tud_psd = psd(tud_data, tud_dwell)
19.
20. tud_maxpos, tud_maxfreq, tud_peakamp = maxfreq(tud_freq, tud_psd, 0.1)
21.
22. tud_mean_amp, tud_sigma_amp = psd_uq(tud_data, tud_dwell, m)

```

< akr2\_experiment\_cases.csv >

```

1. Exp.no.;ISTec file;EPFL file;TUD file;Casename;DC;ISTEC trigger;EPFL trigger
2. 1;AKR2_1_13_KANAL_A_219.csv;exp1-
   card1.txt;;Exp. # 1 | Power [W] 2 | Rot. Freq.[Hz] 2;3.2973;234858;5704
3. 2;AKR2_1_14_KANAL_A_219.csv;exp2-
   card1.txt;Rot_3_0.5Hz;Exp. # 2 | Power [W] 2 | Rot. Freq.[Hz] 0.5;3.2973;83003;2990
4. 3;AKR2_1_15_KANAL_A_191.csv;exp3-
   card1.txt;Rot_3_0.2Hz;Exp. # 3 | Power [W] 2 | Rot. Freq.[Hz] 0.2;3.2973;173076;1747
5. 4;AKR2_1_16_KANAL_A_152.csv;exp4-
   card1.txt;;Exp. # 4 | Power [W] 2 | Rot. Freq.[Hz] 0.2;3.2973;5944;268
6. 5;AKR2_1_17_KANAL_A_165.csv;exp5-
   card1.txt;;Exp. # 5 | Power [W] 1 | Rot. Freq.[Hz] 0.2;4.6866;20656;203
7. 6;AKR2_1_18_KANAL_A_156.csv;exp6-
   card1.txt;;Exp. # 6 | Power [W] 1 | Rot. Freq.[Hz] 0.5;4.6866;11443;97
8. 7;AKR2_1_19_KANAL_A_151.csv;exp7-
   card1.txt;;Exp. # 7 | Power [W] 1 | Rot. Freq.[Hz] 1;4.6866;10626;226
9. 8;AKR2_1_20_KANAL_A_154.csv;exp8-
   card1.txt;;Exp. # 8 | Power [W] 1 | Rot. Freq.[Hz] 2;4.6866;13665;203
10. 9;AKR2_1_22_KANAL_A_174.csv;exp9-
    card1.txt;rot_2W0.5HzDet1;Exp. # 9 | Power [W] 2 | Rot. Freq.[Hz] 1;4.0121;57913;53
11. 10;AKR2_1_23_KANAL_A_163.csv;exp10-
    card1.txt;rot_0.5W0.5HzDet1;Exp. # 10 | Power [W] 0.5 | Rot. Freq.[Hz] 1;3.9388;13128;93
12. 11;AKR2_2_2_KANAL_A_222.csv;exp11-
    card1.txt;Messung1Det1.Asc;Exp. # 11 | Power [W] 1 | tw [s] 0.1 | tm [s] 0.6;5.2768;245486
    ;1861
13. 12;AKR2_2_3_KANAL_A_245.csv;exp12-
    card1.txt;Messung2Det1.Asc;Exp. # 12 | Power [W] 1 | tw [s] 0.4 | tm [s] 0.6;5.2768;347665
    ;1933
14. 13;AKR2_2_4_KANAL_A_166.csv;exp13-
    card1.txt;;Exp. # 13 | Power [W] 1 | tw [s] 1 | tm [s] 0.6;5.2768;25347;2159
15. 14;AKR2_2_5_KANAL_A_162.csv;exp14-
    card1.txt;Messung4Det1.Asc;Exp. # 14 | Power [W] 0.8 | tw [s] 4 | tm [s] 0.6;5.2768;7799;1
    947
16. 15;AKR2_2_6_KANAL_A_90.csv;exp15-
    card1.txt;Messung5Det1.Asc;Exp. # 15 | Power [W] 2 | tw [s] 0.1 | tm [s] 0.6;3.9382;62713;
    1928
17. 16;AKR2_2_7_KANAL_A_81.csv;exp16-
    card1.txt;Messung6Det1.Asc;Exp. # 16 | Power [W] 2 | tw [s] 0.1 | tm [s] 1;4.9191;21797;19
    72
18. 17;AKR2_2_8_KANAL_A_133.csv;exp17-
    card1.txt;Messung7Det1.Asc;Exp. # 17 | Power [W] 1.9 | tw [s] 0.1 | tm [s] 2;4.9191;239426
    ;2036
19. 18;AKR2_2_9_KANAL_A_126.csv;exp18-
    card1.txt;Messung8Det1.Asc;Exp. # 18 | Power [W] 1 | tw [s] 0.4 | tm [s] 2;5.1956;198946;1
    984
20. 19;AKR2_2_10_KANAL_A_78.csv;exp19-
    card1.txt;Messung9Det1.Asc;Exp. # 19 | Power [W] 1 | tw [s] 1 | tm [s] 2;5.391;17809;2299
21. 20;AKR2_2_11_KANAL_A_74.csv;exp20-
    card1.txt;Messung10Det1.Asc;Exp. # 20 | Power [W] 1 | tw [s] 2 | tm [s] 2;5.391;4436;2004
22. 21;AKR2_2_12_KANAL_A_82.csv;exp21-
    card1.txt;Messung11Det1.Asc;Exp. # 21 | Power [W] 1 | tw [s] 4 | tm [s] 2;4.0756;6681;2071
23. 22;AKR2_2_13_KANAL_A_161.csv;exp22-
    card1.txt;Messung12Det1.Asc;Exp. # 22 | Power [W] 2 | tw [s] 0.1 | tm [s] 1;6.1875;6461;21
    2
24. 23;AKR2_2_14_KANAL_A_123.csv;exp23-
    card1.txt;Messung13Det1.Asc;Exp. # 23 | Power [W] 2 | tw [s] 1 | tm [s] 1;4.255;144294;243
    5
25. 24;AKR2_2_15_KANAL_A_131.csv;exp24-
    card1.txt;Messung14Det1.Asc;Exp. # 24 | Power [W] 2 | tw [s] 0.4 | tm [s] 0.4;4.255;225023
    ;695
26. 25;AKR2_2_16_KANAL_A_159.csv;exp25-
    card1.txt;Messung15Det1.Asc;Exp. # 25 | Power [W] 2 | tw [s] 0.4 | tm [s] 0.4;4.255;9055;9
    3
  
```

27. 26;AKR2\_2\_17\_KANAL\_A\_127.csv;exp26-  
card1.txt;Messung16Det1.Asc;Exp. # 26 | Power [W] 2 | tw [s] 2 | tm [s] 0.4;4.255;7630;504
28. 27;AKR2\_2\_18\_KANAL\_A\_75.csv;exp27-  
card1.txt;;Exp. # 27 | Power [W] 2 | tw [s] 2 | tm [s] 0.4;4.255;4098;723